INTERNATIONAL JOURNAL FOR NUMERICAL METHODS IN FLUIDS
Int. J. Numer. Meth. Fluids 2007; **54**:175–206
Published online 28 November 2006 in Wiley InterScience (www.interscience.wiley.com). DOI: 10.1002/fld.1396

Numerical study of transitional separated–reattached flow over surface-mounted obstacles using large-eddy simulation

Ibrahim E. Abdalla[1,*,†], Malcolm J. Cook[1] and Zhiyin Yang[2]

[1]*Institute of Energy and Sustainable Development, De Montfort University, Leicester LE1 9BH, U.K.*
[2]*Department of Aeronautical and Automotive Engineering, Loughborough University, Leicester LE11 3TU, U.K.*

SUMMARY

Large-eddy simulation (LES) of transitional separating–reattaching flow on a square surface mounted obstacle has been performed. The Reynolds number based on the uniform inlet velocity and the obstacle height is 4.5×10^3. A dynamic subgrid-scale model is employed in this work. The mean LES results compare favourably with the available experimental and direct numerical simulation (DNS) data. Extensive analysis of the time series signals of the velocity and pressure fields at different locations including positions close to solid surfaces, at the centre and edge of the separated–reattached boundary layer using the windowed Fourier transform (WFT) and the wavelet transform was performed. The spectra analysis revealed the nature of the amplified frequencies at all the important locations of the flow field. Excited modes that could be due to the movement (shedding) of large-scale structures and pairing of such types of structures are identified. A clear frequency peak was captured just upstream of the separation line. The value of the frequency peak and the low percentage of the back flow velocity compared to the freestream velocity in the current case strongly support the idea that this amplified frequency is most likely due to the Kelvin–Helmholtz (K–H) instability mechanism of the shear layer forming in the boundary of the small upstream separated region rather than being attributed to the flapping of the shear layer.

Received 16 May 2006; Revised 27 September 2006; Accepted 3 October 2006

KEY WORDS: large-eddy simulation; transition to turbulence; coherent structures; wavelet; shedding

1. INTRODUCTION

The flow over a surface-mounted obstacle is considered as a useful benchmark for many environmental applications including the study of air pollution, wind loading on tall buildings, meteorology, wind energy applications, flow over road embankments in addition to its wide application in the

*Correspondence to: Ibrahim E. Abdalla, Institute of Energy and Sustainable Development, De Montfort University, Leicester LE1 9BH, U.K.
†E-mail: iabdalla@dmu.ac.uk

turbo-machinery industry and aerodynamics of road vehicles and aircraft. The flow over a surface-mounted obstacle constitutes two basic study cases for *strongly* separated flows occurring both upstream and downstream of the obstacle. The basic characteristics of such flow configurations are the length of the recirculating region upstream and downstream of the obstacle. The length depends on the ratio of the boundary layer thickness of the approaching flow to the obstacle height and also the geometry of the obstacle itself.

The obstacle flow is influenced by three parameters. The Reynolds number; the blockage ratio (ratio of the channel height to the obstacle height H/h) and the aspect ratio (of the obstacle l/h). Previous experimental and computational studies for the obstacle case are associated with the basic features of the flow in a fully turbulent environment. Bergeles and Athanassiadis [1] and Castro [2] investigated the influence of the obstacle aspect ratio (l/h) on the mean reattachment length while Durst and Rastogi [3] performed both experimental and numerical studies to investigate the effect of varying the blockage ratio from 2 to ∞ (open test section) while keeping l/h constant. Dimaczek *et al*. [4] studied the flow around a surface mounted obstacle with different aspect and blockage ratios including $l/h=1.0$ at high Reynolds number ($Re_h=42\,500$) in fully developed channel flow.

Tropea and Gackstatter [5] experimentally investigated the flow over a fence and a block mounted in a fully developed channel flow as a function of the Reynolds number, blockage ratio and length-to-height ratio. The experiments were conducted in a channel for a Reynolds number range $150\leqslant Re\leqslant 4500$ (based on the obstacle height h). Three blockage ratios were employed, $H/h=4$, 2, and 1.33. Regarding the effect of Reynolds number, Tropea and Gackstatter [5] identified three characteristic regions: the laminar region characterized by a steady increase in x_R/h with Reynolds number; the transitional region identified by an abrupt reduction in x_R/h in some cases, a partial recovery; and a turbulent region in which x_R/h does not vary much. For the fence geometry with a blockage ratio $H/h=4$ the mean reattachment length varied in the range $8.5\leqslant x_R/h\leqslant 17.25$ and for the square block case $5\leqslant x_R/h\leqslant 16$.

Computational simulation for the obstacle and fence case includes Yang and Ferziger [6] who performed both a direct numerical simulation (DNS) and large eddy simulation (LES) studies for an obstacle immersed in a turbulent channel flow (employing a periodic boundary condition along both the stream and spanwise directions) at $Re=3210$ based on the mean velocity above the obstacle and the obstacle height. Orellano and Wengle [7] conducted both DNS and LES simulation for a turbulent boundary layer over a fence at low Reynolds number ($Re=3000$) based on the fence height h. They obtained a mean reattachment length of $13.2h$ and good agreement between the DNS, LES and the experimental data of Larsen [8] at the same value of Reynolds number and for the case without user manipulation (excitation). Lee and Bienkiewicz [9] employed the Smagorinsky model to study the flow of an obstacle in a fully turbulent channel flow at $Re=40\,000$ (based on the obstacle height) with a blockage ratio of 2. They predicted a mean reattachment length $x_R/h=6.42$. However, the Smagorinsky model showed discrepancy when compared to the experimental data of Dimaczek *et al.* [4] and the LES data of Werner and Wengle [10] for a similar geometry in a similar turbulent channel environment at $Re=42\,500$ especially in the rms of the U-velocity. Werner and Wengle [10] predicted a mean reattachment length of $7.1h$.

It is well established that separated–reattached boundary layers exhibit two characteristic shedding frequencies: shedding at low frequency attributed to the flapping of the separated shear layer, and shedding at a band of higher frequencies which is a result of movement (shedding) of large-scale structures dominating the separated boundary layer. The above features have been extensively studied for separated–reattached flows for different geometries. The blunt leading-edge plate

DOI: 10.1002/fld

geometry case has been the subject of many investigations and both experimental and computational studies have been performed at high Reynolds number (Kiya and Sasaki [11] and Cherry *et al.* [12]) and at low Reynolds number (Tafti and Vanka [13] and Abdalla and Yang [14]). The characteristic shedding frequency which is assumed to be due to the shedding of large-scale vortices from the separation bubble in these studies is in the range of $fx_R/U_\infty = 0.7$–0.8. In addition to this, others have identified a lower frequency content of order $fx_R/U_\infty = 0.15$ which they attributed to the flapping of the shear layer [11–13].

Cherry *et al.* [12], Castro and Haque [15], and Laura *et al.* [16] detected both the low and high frequency modes of unsteadiness for separated flow behind a normal flat plate with a long central splitter plate. However, Ruderich and Fernholz [17] observed no dominant frequencies in their power spectra for the same flow configuration, which led them to believe that there was no flapping of the reattaching shear layer.

In the backward-facing step flow, both the frequency modes were detected in velocity measurements of Eaton and Johnston [18]. They argued that the observed low-frequency motion on the backward-facing step is likely to be a consequence of an instantaneous imbalance between the entrainment rate from the recirculation zone and the reinjection near the reattachment line. In the backward-facing step experiment by Lee and Sung [19] the two modes of frequency were also detected in the measured auto-spectra of surface pressure close to separation line.

For the surface mounted obstacle, the phenomenon has not been explored in as much details. Only Dimaczek *et al.* [4] has investigated the energy spectra for the wall pressure and the streamwise velocity fluctuations of a surface mounted obstacle similar to the current case. They did not observe the low-frequency peak in their work but the pressure spectra showed a broad peak at higher frequency band ($fx_R/U_0 \approx 1.0$) and they believe that the restriction caused by the obstacle might have contributed to widening the spectral distribution considerably.

Castro [20] conducted a numerical study of the instability of laminar symmetric separated wakes. He concluded that if the backflow velocity is small compared to the free-stream velocity (typically less than 20%), the low-frequency component is generally absent. His conclusion was supported by other experimental and DNS studies including the DNS study of Alam and Snadham [21] who reported a maximum negative velocity above 15% of the free-stream velocity for less than 1% of the time but no low-frequency component was observed. In a recent investigation for a separated boundary layer behind a fence geometry, Orellano and Wengle [7] presented the spectra for 9 locations (unmanipulated case) including 3 points upstream of the separation and one point after reattachment region. Their results did not reveal the low-frequency mode and they did not identify a dominant peak immediately after separation. However, with increasing distance downstream the separation line they noticed amplified frequencies although no clear peak is apparent.

Almost all the experimental and numerical work discussed above deal with turbulent separation at high Reynolds number with the exception of the simulation of Tafti and Vanka [13] and Abdalla and Yang [14]. In fact, Cherry *et al.* [12] concluded that the low-frequency phenomena is an integral feature of turbulent separation. For a transitional flow for the same geometry of Kiya and Sasaki [11] and Cherry *et al.* [12], Abdalla and Yang [14] performed an extensive study of the velocity and pressure spectra and no traces of the low-frequency peak was detected. The dynamic of the current separated–reattached boundary layer is slightly different from the blunt plate geometry for which the phenomena is extensively documented but bear many similarities to the fence case. Two unanswered questions remain: will the change in the geometry impose any difference on the low-frequency unsteadiness or will the laminar separation serve as a filter to absorb or dampen it?; could the shedding behaviour of the recirculation region upstream of the obstacle (the standing

DOI: 10.1002/fld

vortex), which distinguish this case from all the case studies cited above, affect the low-frequency motion?

This paper reports on LES models used to study the transitional flow over a surface-mounted (square block) obstacle. The prime objectives were to study the physics of transition and perform extensive analysis of the turbulence spectra at different locations within the computational domain to identify the characteristic features of the spectra. Such features and their relationship with the large-scale structures dominating the flow are discussed.

The paper contains details of the numerical model used (Section 2), comparison of the mean flow variables with experimental results (Section 3), spectral analysis and discussion of the associated coherent structures (Section 4) and conclusions of the study (Section 5).

2. GOVERNING EQUATIONS AND THE NUMERICAL METHOD

The filtered equation expressing conservation of momentum in a Newtonian incompressible flow is normally written in an explicitly conservative form

$$\partial_t(\bar{u}_i) + \partial_j(\overline{u_i u_j}) = -\partial_i \bar{P} + 2\partial_j(\bar{S}_{ij}) \tag{1}$$

the strain $\bar{S}_{ij}$ is

$$\overline{S}_{ij} = \tfrac{1}{2}(\partial_i \bar{u}_j + \partial_j \bar{u}_i) \tag{2}$$

$\bar{P}$ is the physical pressure divided by density.

The mass conservation law is expressed by the zero divergence of the velocity field

$$\partial_i \bar{u}_i = 0 \tag{3}$$

The equation for pressure is developed by taking the divergence of (1)

$$\partial_i \partial_t(\bar{u}_i) + \partial_i \partial_j(\overline{u_i u_j}) = -\partial_i \partial_i \bar{P} + 2\partial_i \partial_j(\nu \bar{S}_{ij}) \tag{4}$$

ν is the total viscosity. By using continuity (3) one finally obtains

$$\partial_i \partial_j \bar{P} = \Delta^2 \bar{P} = \partial_i H_i \tag{5}$$

where

$$H_i = \partial_j(-\overline{u_i u_j} + 2\nu \bar{S}_{ij}) \tag{6}$$

Equation (5) is particularly suitable for the time accurate computation of the pressure in an incompressible flow simulation using linear differencing. The equation can be Fourier transformed in z (a very rapid computational task) to obtain a set of decoupled equations, which in Cartesian form are given by

$$\frac{\partial^2 \tilde{P}}{\partial^2 x} + \frac{\partial^2 \tilde{P}}{\partial^2 y} - k_z^2 \tilde{P} = \tilde{R} \tag{7}$$

This process can be performed even when the z derivatives are replaced by the finite-difference formulae, provided z in the simulation is periodic and has an even uniform mesh. The Fourier

DOI: 10.1002/fld

transform requires an even and multiple of 4 mesh in order to be performed. For example, the second-order central scheme on an even uniform mesh

$$\frac{\partial^2 P}{\partial^2 z} = \frac{P_{n-1} - 2P_n + P_{n+1}}{\Delta z^2} \tag{8}$$

can be discrete Fourier transformed to give

$$-\frac{4\tilde{P}}{\Delta z^2} \sin^2(K_z/2) = -K_z^2 \tilde{P} \tag{9}$$

where

$$K_z = \frac{2\sin(K_z/2)}{\Delta z} \tag{10}$$

and K_z is the usual discrete Fourier wave number.

The two-dimensional equation (9), one for each value of K_z can be solved very quickly even when the geometry is complex as long as it is homogeneous in one direction.

The subgrid-scale stress term

$$\tau_{ij} = \overline{u_i u_j} - \bar{u}_i \bar{u}_j \tag{11}$$

represents the contribution from the subgrid scales and must be modelled. In the present study, the dynamic model (Germano *et al.* [22], Lilly [23]) has been applied.

Applying the base (Smagorinsky [24]) model at both filter scales

$$\tau_{ij} - \tfrac{1}{3}\delta_{ij}\tau_{kk} = -2C\Delta^2 \mid \bar{S} \mid \bar{S}_{ij} \tag{12}$$

$$T_{ij} - \tfrac{1}{3}\delta_{ij}T_{kk} = -2C\widehat{\Delta}^2 \mid \widehat{\bar{S}} \mid \widehat{\bar{S}}_{ij} \tag{13}$$

Using the Germano identity (Germano *et al.* [22]) and following Lilly [23], C can be evaluated as

$$C = \frac{1}{2}\frac{L_{ij}M_{ij}}{M_{ij}M_{ij}} \tag{14}$$

This evaluation of C differs from that of Germano *et al.* [22] expressed as

$$C = \frac{1}{2}\frac{L_{ij}\bar{S}_{ij}}{M_{ij}\bar{S}_{ij}} \tag{15}$$

In the current simulation C is defined as

$$C = \frac{1}{2}\frac{\langle L_{ij}M_{ij}\rangle}{\langle M_{ij}M_{ij}\rangle} \tag{16}$$

where the angle brackets represent an average over the homogeneous z in which C will not change. The resulting C is a function of time and the inhomogeneous co-ordinates x and y.

In finite volume calculations the test-filtered flow quantities can be computed by spatial averaging of the calculated large scale variables over a few grid cells (typically 9 in the current study).

The explicit second-order Adams–Bashforth scheme is used for the momentum advancement except for the pressure term. A disadvantage of explicit schemes is the restriction imposed on the

DOI: 10.1002/fld

magnitude of the time step to be used. To ensure numerical stability for explicit schemes the time step must be small enough to satisfy a certain stability criteria. In the code used here, both the Courant–Friedrich–Lewy (CFL) number defined as:

$$\mathrm{CFL} = \Delta t \left(\frac{|u|}{\Delta x} + \frac{|v|}{\Delta y} + \frac{|w|}{\Delta z} \right) \tag{17}$$

and the diffusion stability (DFS) number, defined as

$$\mathrm{DFS} = v_t \Delta t \left(\frac{1}{\Delta x^2} + \frac{1}{\Delta y^2} + \frac{1}{\Delta z^2} \right) \tag{18}$$

should be kept below a maximum value of 0.35 to ensure a solution free from any numerical instability (the CFL number in the current case is of order 0.18 and the DFS number is much lower). For this method, the CFL number usually fluctuates around this value (0.18), however, other LES codes adopt the method of fixing the CFL number and estimate the physical magnitude of the time step prior to each time step. It is worth pointing out that the value of these two parameters are grid dependent when LES is used, especially the DFS number which is found to increase considerably with mesh refinement near a solid boundary, hence demanding smaller time steps.

Due to the use of explicit schemes in solving the momentum equation, it is very important to find an efficient numerical method for solving the Poisson equation of pressure (Equation (5)). The code employs the multigrid method which is considered favourable for unsteady flow simulations (Ferziger and Peric [25]).

The spatial discretization is the second-order central differencing scheme which is widely used in LES owing to its non-dissipative and conservative properties. The code employs the conventional staggered grid system (Harlow and Welch [26]). The control volume cell for the pressure does not coincide with control volume cells for velocities.

2.1. Code validation

The code was validated against standard fully developed channel flow [27] with the Smagorinsky model [24]. The dynamic model was used to study the physics of transition over a blunt plate geometry aligned horizontally to an incoming laminar flow and validated with experimental work [14, 28–30].

2.2. Flow configuration, mesh and boundary conditions

Figure 1 shows the computational domain and mesh used in the study. Two simulations were performed for the obstacle case. In the first simulation $288 \times 128 \times 64$ cells along the streamwise, wall-normal and spanwise directions, respectively, were employed. The inflow boundary is at $5h$ distance from the upstream side of the obstacle while the outflow boundary is at $30h$ measured from the obstacle upstream side. From previous experience with related flows [28–30] we found that between 4 and $5H$ is sufficient to avoid any interaction of the inflow with that close to the leading edge of the obstacle. Depending on the length of the predicted mean reattachment length, locating the outflow boundary $30h$ downstream of the separation edge with the fine mesh used was found to be adequate in ensuring no interaction with the downstream flow field. The lateral boundary is at $8h$ distance from the lower surface ($y = 0$), corresponding to a blockage

DOI: 10.1002/fld

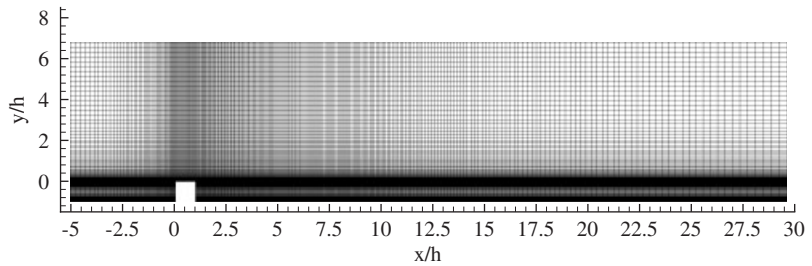

Figure 1. The computational domain showing the mesh used in resolving the flow over a surface-mounted obstacle for the two simulations.

ratio of 8 for the first simulation. The spanwise dimension of the domain is $4h$. Yang and Voke [31] performed simulations using a spanwise dimension of $2h$ without any appreciable change in the behaviour of the flow (less than 5% difference in terms of averaged statistics for both mean and turbulence stress when compared to the case with spanwise dimension of $4h$). A free-slip but impermeable boundary is applied at the lateral boundary. In the spanwise direction, the flow is assumed to be statistically homogeneous and periodic boundary conditions are used. No-slip boundary conditions are used at all other walls. At the inflow boundary, a uniform velocity profile is applied and the Reynolds number based on the inflow velocity and obstacle height is 4500. At the outflow boundary, a convective boundary condition is applied. Non-uniform grid distributions are used in the x- and y-direction with finer resolution in the vicinity of the obstacle. The reason for refining the grid in this region is to resolve the standing vortex which forms upstream of the obstacle, the shear layers that develop at the separation line and the recirculation region downstream of the obstacle. A uniform grid distribution is used in the spanwise direction. In terms of wall units based on the friction velocity downstream of reattachment at $x/h = 27$, the streamwise mesh sizes vary from $\Delta x^+ = 6.77$ to $\Delta x^+ = 43.04$, while $\Delta z^+ = 10.625$ and at the wall $\Delta y^+ = 1.28$. The time step used in this simulation is 4.75×10^{-6} s $(0.001425(h/U_0))$. The simulation ran for 129 000 time steps equivalent to more than 5 flow passes through the domain (or residence times) to allow the transition and turbulent boundary layer to be established, i.e. the flow to have reached a statistically stationary state. The averaged results were gathered over a further 249 900 steps, with a sample taken every 10 time steps (24 990 samples) averaged over the spanwise direction too, corresponding to more than 10 flow passes or residence times.

The second simulation used $320 \times 220 \times 64$ cells along the streamwise, wall-normal and spanwise directions, respectively. The computational domain was made slightly shorter than the previous simulation and the lateral boundary is at $y = 15h$ distance from the lower surface ($y = 0$) resulting in a blockage ratio of 15. In terms of wall units based on the friction velocity downstream of reattachment at $x/h = 23$, the streamwise mesh sizes vary from $\Delta x^+ = 6.09$ to $\Delta x^+ = 19.988$, while $\Delta z^+ = 10.96$ and at the wall $\Delta y^+ = 1.14$. The time step used in this simulation is 1.5×10^{-6} $(0.010125(h/U_0))$. The simulation ran for 95 000 time steps to allow the transition and turbulent boundary layer to be established, i.e. the flow to have reached a statistically stationary state. The averaged results gathered over 35 000 steps, with a sample taken every 10 time steps (3500 samples) averaged over the spanwise direction too, shows no significant changes in the mean reattachment length from the previous simulation. For this reason and the larger run time required for the second simulation, results from the first simulation are presented here.

DOI: 10.1002/fld

3. RESULTS AND DISCUSSION

The current LES results are compared with the experimental data by Tropea and Gackstatter [5] whose experimental work addresses the obstacle and fence geometry in the transitional range of Reynolds numbers. The work of Tropea and Gackstatter [5] is mainly concerned with the basic parameter of this flow which is the variation of the mean reattachment length with blockage ratio and Reynolds number. For this reason, the LES data is also compared with the experimental work of Larsen [8] and the DNS data of Orellano and Wengle [7]. Both studies deal with a separated boundary layer behind a fence geometry at Reynolds number of 3000 based on the fence height with a blockage ratios of 5 for the DNS of Orellano and Wengle [7] and 7.5 for the experimental work of Larsen [8]. Comparison of the mean variables are presented at positions downstream of the separation line since the separated boundary layer dynamics in the two cases is similar. The main difference between this case and the current transitional LES simulation is the fully turbulent separation in [7, 8].

3.1. Mean flow variables

3.1.1. Mean reattachment length. An important parameter characterizing a separated–reattached flow is the time mean position of the reattachment. The method used here to determine the mean reattachment location is described by Hung *et al.* [32] in their DNS study for a backward-facing step flow. The method involves determining the location at which the mean velocity $\overline{U} = 0$ at the first grid point away from the wall. The time averaged velocity vectors are shown in Figure 2. For the current transitional separated-boundary layer flow, the time averaged results is similar to a steady laminar separated flow, but with different bubble shape and separation length. Figure 2(a) shows clearly one separation bubble starting from the separation line (the upstream side of the obstacle) reattaching at a downstream location $x/h \approx 15.42$ giving a mean reattachment length of $\approx 15.5h$ as shown in Figure 3. The second simulation with the finer mesh and blockage ratio of 15 produced the same mean reattachment length—an indication of the fact that the blockage ratio of 8 is satisfactory in eliminating the effect of the blockage ratio and the first mesh is fine enough to produce the same quality mean value compared to the second. For the obstacle case, Tropea and Gackstatter [5] reported a mean reattachment length of $15.5h$ at $Re_h \approx 1000$. This value of Re is within the transitional range of their experiment. But bearing in mind that the experimental work of Tropea and Gackstatter [5] was done under fully developed turbulent channel flow, then the level of free stream turbulence is higher than the current case. It is well documented that free stream turbulence and turbulent separation reduces the mean reattachment length compared with transitional flow conditions [2, 30]. Taking into consideration the fact that the experiment of Tropea and Gackstatter [5] was conducted for a fully developed channel flow, the predicted mean reattachment length is expected to be slightly longer than that reported by the experiment. However, the agreement in predicting this parameter is good. Other experimental and simulation results for both the block and fence geometry have shown similar results. Bergeles and Athanassiadis [1] reported a value of $x_R/h = 11$ for a turbulent boundary layer of thickness $0.48h$ while Tillman's [33] measurement for a turbulent thick boundary layer ($3.3h$) is $x_R/h = 12.5$. Durst and Rastogi [3] reported a value of $x_R/h = 16$ also under a turbulent boundary layer condition. Similar scatter was reported for the fence geometry. Tropea and Gackstatter [5] reported a value of $x_R/h = 17$ under transitional flow conditions and the DNS study of Orellano and Wengle [7] reported $x_R/h = 13.2$ (12.8 for the LES with Smagorinsky model). Larsen [8] reported a value of

DOI: 10.1002/fld

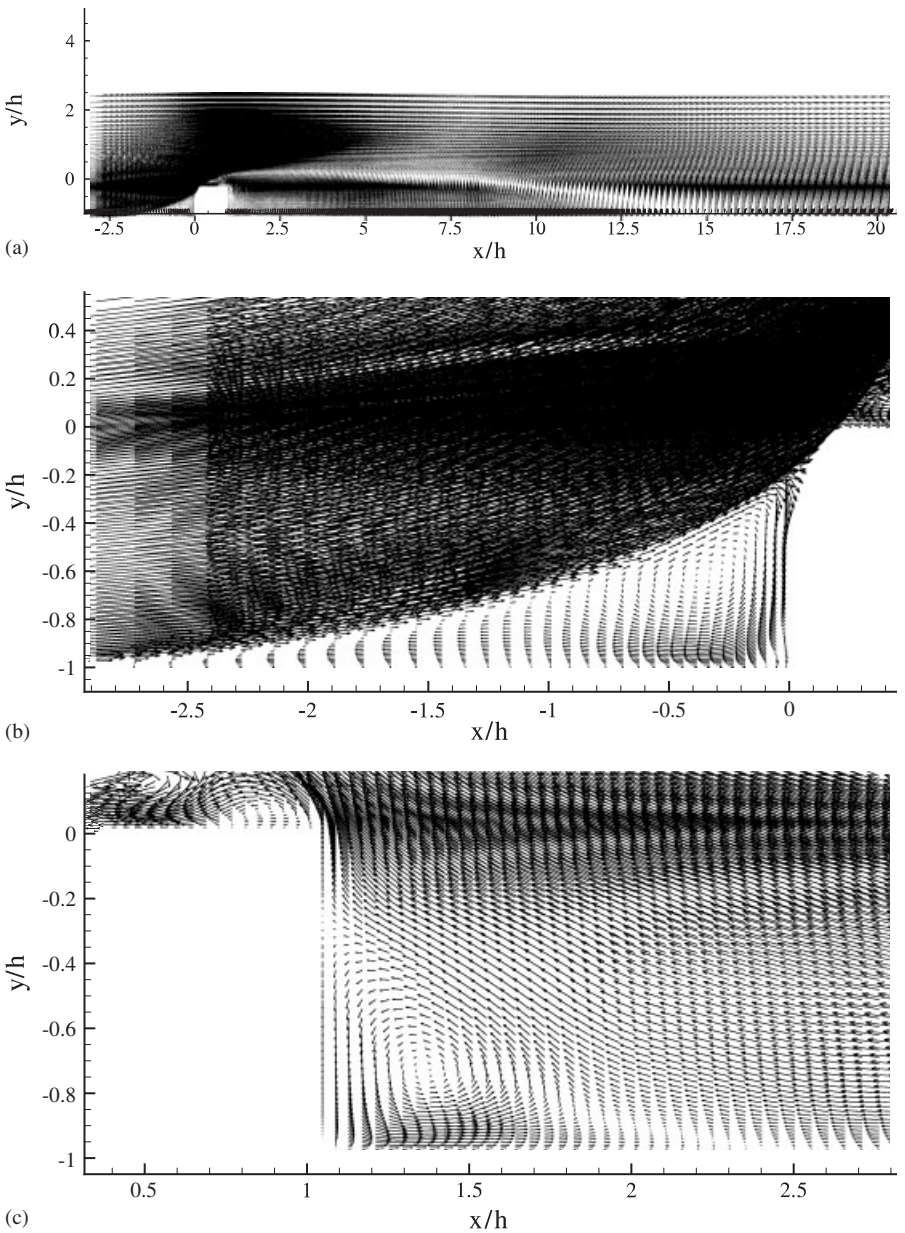

Figure 2. (a) Time-averaged mean vectors showing the mean reattachment length; and (b) and (c) are enlarged images for the region upstream and immediately downstream of the obstacle, respectively.

$x_R/h = 11.7$ from his experimental work which is conducted under a large turbulence intensity. Comparing the current LES results with the scatter of the results above, it is clear that the LES prediction is within the range for the current transitional flow.

DOI: 10.1002/fld

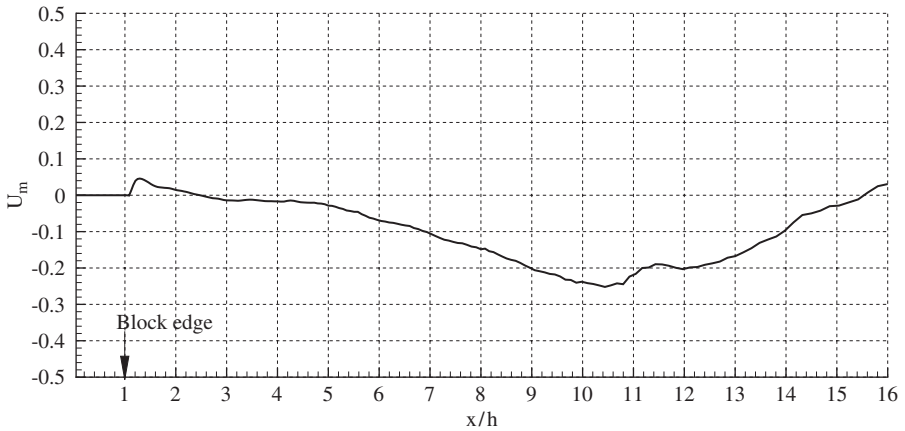

Figure 3. Streamwise mean velocity profile at the first cell from the solid surface along the streamwise direction.

In addition to the main recirculation zone downstream of the obstacle, the LES results show a secondary separation zone immediately downstream of the obstacle (at the lower corner) of order $2.6h$ length (Figure 2(c)) and $0.65h$ height. The DNS of Orellano and Wengle [7] reported $2.7h$ length and the LES $2.6h$ for this separation zone. For a fully turbulent channel flow under high blockage ratio, Yang and Ferziger [6] reported a value of $1.76h$ and height $0.36h$ from an LES simulation which clearly illustrates the effect of blockage ratio and the turbulent separation effect. In addition to the main separation zone downstream, the LES shows a further zone upstream of the obstacle of order $2.5h$ length and $0.75h$ height (Figure 2(b)) compared to $1.51h$ length and $0.37h$ of the LES of Yang and Ferziger [6]. The DNS of Orellano and Wengle [7] reported $2.0h$ length and the LES $1.9h$ for this separation zone. It is usually termed the standing vortex and it is a characteristic of the surface-mounted obstacle flow. The LES of Yang and Ferziger [6] also showed a small recirculation zone at the lower corner upstream of the obstacle which was also captured in the current LES study as shown in Figure 2(b).

3.1.2. Mean velocity field. Due to the scarcity in the data from almost all the papers reporting the separated boundary layer of an obstacle (including Tropea and Gackstatter [5]), the LES results are also compared with the experimental data of Larsen [8] and the DNS data of Orellano and Wengle [7] of a separated boundary layer behind a fence geometry.

Figure 4 compares the mean streamwise velocity distribution $\overline{U}/U_0$ at 6 locations downstream of the separation line with the experimental data of Tropea and Gackstatter [5] (available only at 3 locations), Larsen [8] and the DNS data of Orellano and Wengle [7]. The results show good agreement with the data of Larsen [8] and the DNS data of Orellano and Wengle [7]. The free-stream velocities of the data from Tropea and Gackstatter [5] are bigger than those predicted by the LES and the other two results, and peak at lower y-values. One of the reasons for this discrepancy is the difference in blockage ratio used by Tropea and Gackstatter [5] which is very low (2, 5 in the case of Orellano and Wengle [7] and 8 for the current LES).

Profiles of the rms streamwise velocity, u_{rms}, normalized by U_0, at the same six stations are shown in Figure 5. The agreement between the LES results and the data of Larsen [8] and the

DOI: 10.1002/fld

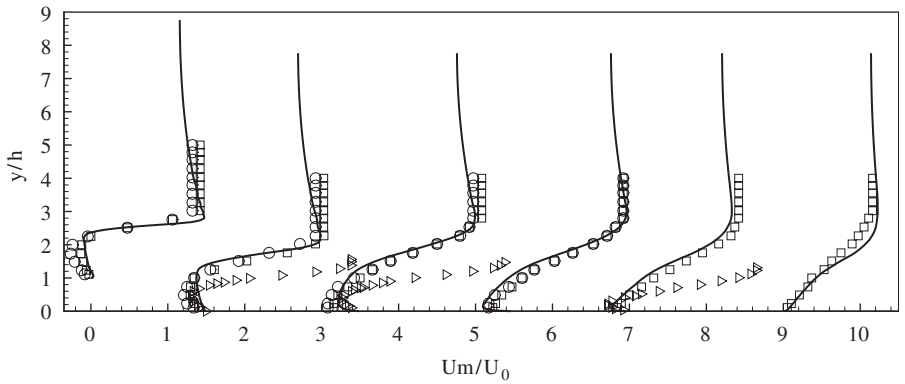

Figure 4. Profiles of mean streamwise velocity Um/U_0 at six streamwise locations measured from the separation line (leading edge). Left to right $x/x_R = 0.05, 0.2, 0.4, 0.6, 0.8, 1.025$. Also shown are measurements by Tropea and Gackstatter [5] (triangle), Larsen [8] (square) and the DNS data of Orellano and Wengle [7] (circle) at $Re = 3000$.

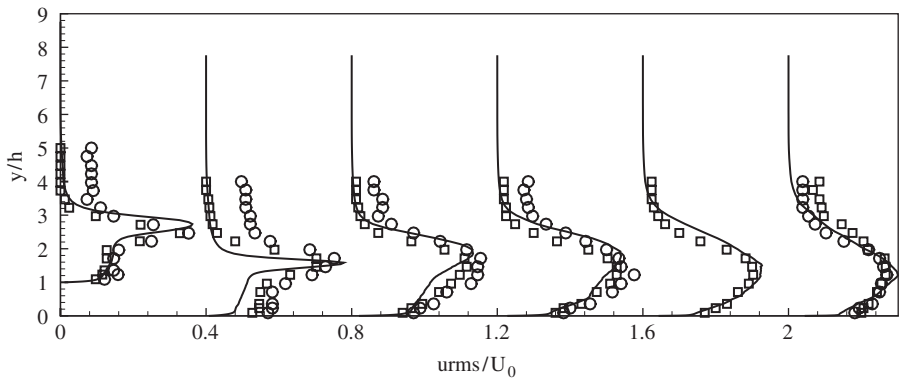

Figure 5. Profiles of mean streamwise turbulent intensity u_{rms}/U_0 at six streamwise locations measured from the separation line (leading edge). Left to right $x/x_R = 0.05, 0.2, 0.4, 0.6, 0.8, 1.025$. Also shown are measurements by Larsen [8] (square) and the DNS data of Orellano and Wengle [7] (circle) at $Re = 3000$.

DNS data of Orellano and Wengle [7] is encouraging. No measured data were presented by Tropea and Gackstatter [5].

Figure 6 shows the profiles of v_{rms}/U_0 at the same six locations. The current LES results show favourable agreement with the DNS data of Orellano and Wengle [7] (no data from Larsen [8] and Tropea and Gackstatter [5] is available). One of the reasons for the difference between the LES and DNS results (especially in the peak value at positions at $x/x_R = 0.4$, 0.6, and 0.8) is thought to be due to the difference in the blockage ratio. The subgrid scale turbulence model used in the LES could also contribute to this difference.

It is valuable to mention at this point the importance of the parameter δ/h on which the significance of the blockage ratio depends as reported by Castro and Fackrell [34]. Here, δ is the

DOI: 10.1002/fld

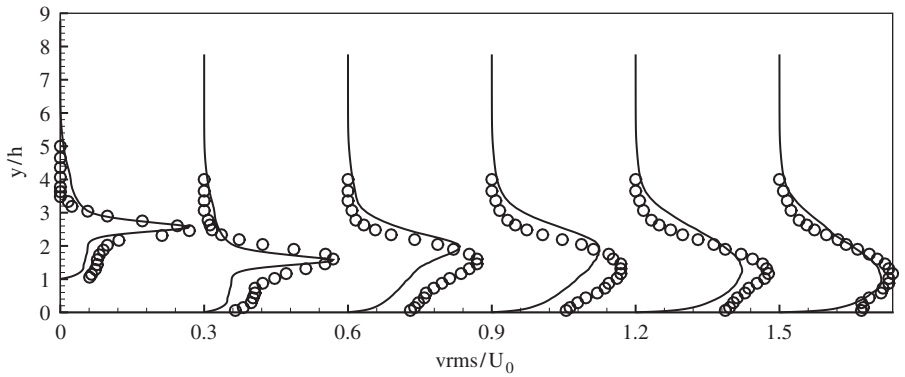

Figure 6. Profiles of mean streamwise turbulent intensity v_{rms}/U_0 at six streamwise locations measured from the separation line (leading edge). Left to right $x/x_{\text{R}} = 0.05, 0.2, 0.4, 0.6, 0.8, 1.025$. Also shown are the DNS data of Orellano and Wengle [7] (circle) at $Re = 3000$.

thickness of the boundary layer which would be present at the obstacle position in its absence. As an example, measuring the drag coefficient in a fence flow arrangement, Castro and Fackrell [34] found that the drag-coefficient deviation is significant at low values of fence-height to boundary-layer thickness and relatively insignificant at high values of fence-height to boundary-layer thickness. It would have been more useful to compare the effect of blockage ratio and the ratio δ/h for the current study with the experimental and DNS data used for validating the results. For the current LES study, no simulation in the absence of the obstacle was performed to evaluate δ although it is possible to estimate the ratio as $0.16 \leqslant \delta/h \leqslant 0.258$ based on the analytical solution for (laminar/turbulent) boundary layer equations in zero pressure gradient (flat plate flow) with Reynolds number based on the distance from the obstacle leading edge. There is a lack of data for δ for both the experimental and DNS data used for comparison. However, taking into consideration the similar values of both Reynolds number and blockage ratio for [7, 8], it is not expected that the difference in blockage ratio will be the only reason for the difference between the results discussed above.

3.2. Transition process

The flow separates at the block leading edge and the boundary layer develops downstream and becomes fully turbulent long before reaching the out-flow boundary (Figures 7(a) and (b)). In the earliest stages of the simulation, a steady separation bubble appears at the separation line (the leading-edge) and takes a 2D form similar to that found for a laminar separation bubble at low Reynolds number. The stable bubble moves along the short obstacle width (h) while growing in size. Upon leaving the trailing edge of the block, another bubble takes its place at the leading edge. Eventually, many smaller (2D) bubbles were observed to leave the block edge and travel downstream. These bubbles are kept far from the lower surface boundary and hence they maintain their coherence and two-dimensionality for a considerable distance downstream of the separation line. Pairing of these kinds of vortices to form a larger vortex is illustrated in the pressure field (Figure 7(b)). In this laminar fashion, large-scale structures resulting from the pairing of smaller vortices are detached and shed from the main body of the bubble as seen from the pressure field (Figure 7(b)).

DOI: 10.1002/fld

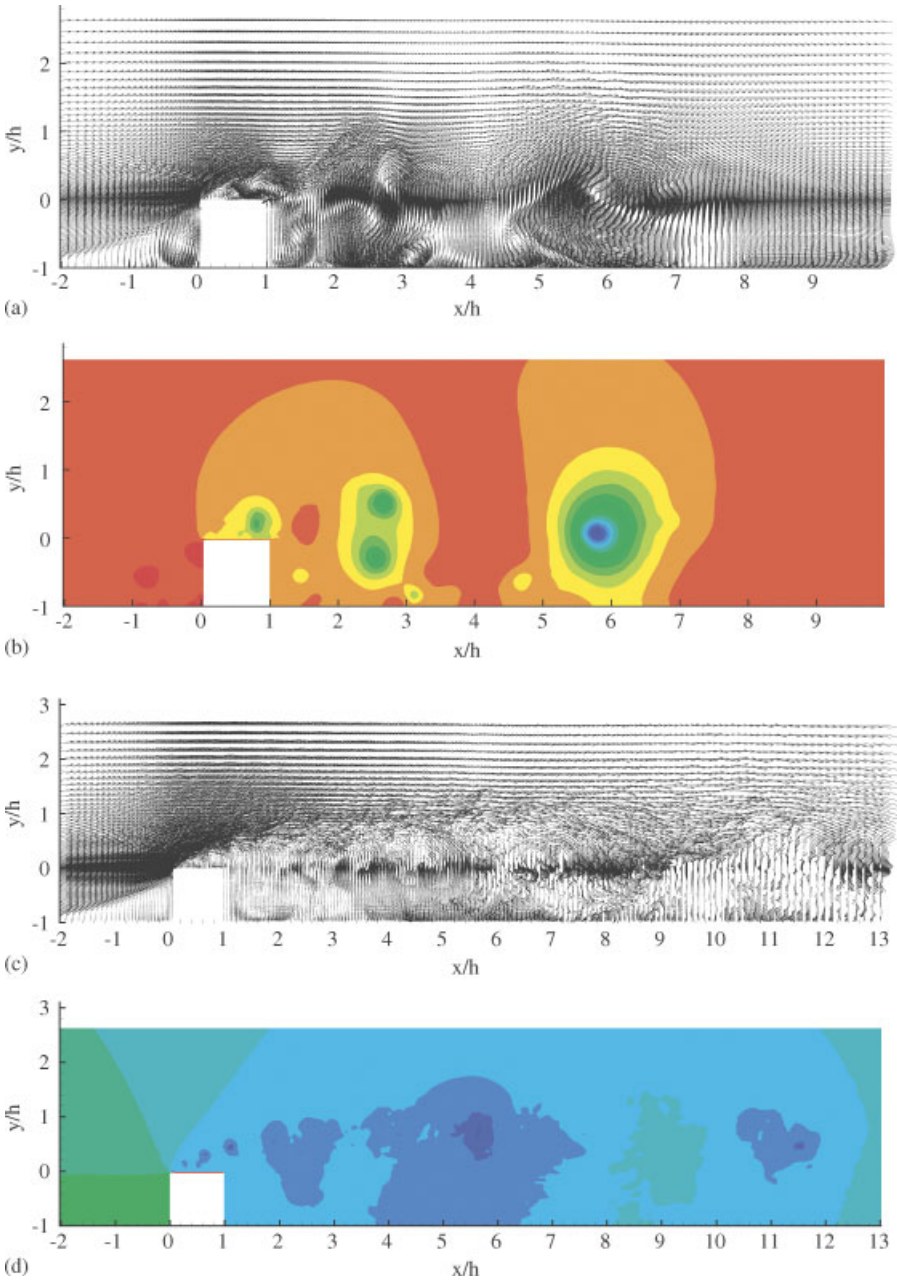

Figure 7. Instantaneous velocity vectors and the corresponding pressure contours in the (x, y) plane: (a,b) at $t = 0.057$ s; and (c,d) at $t = 0.44175$ s.

DOI: 10.1002/fld

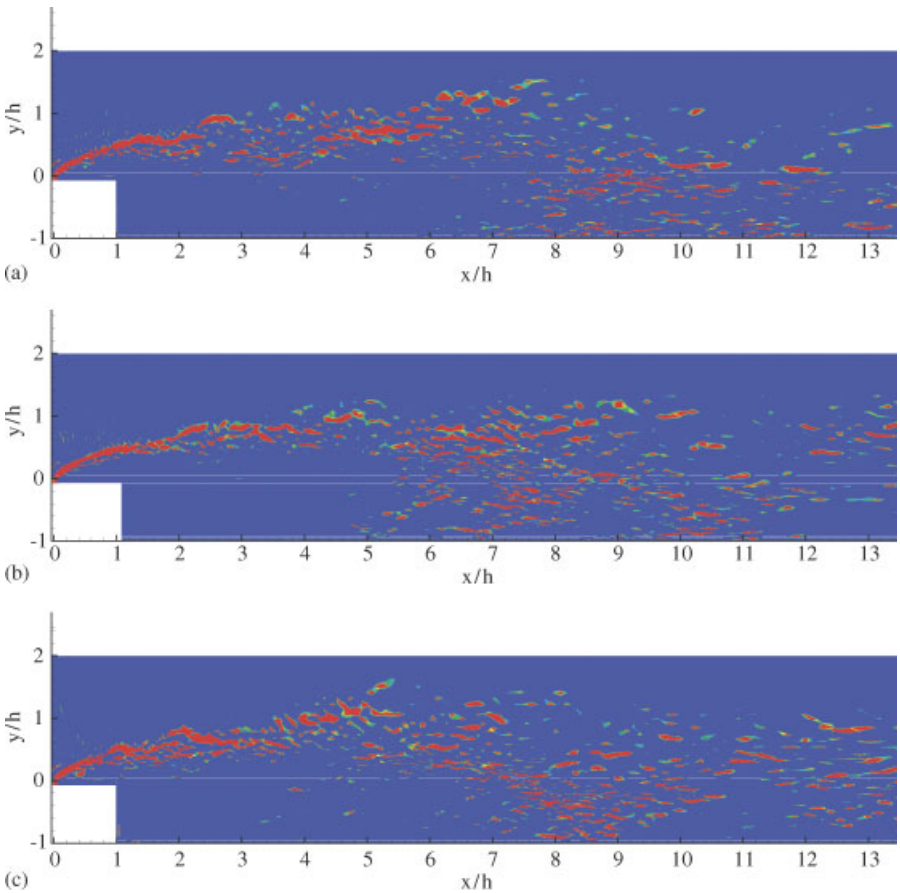

Figure 8. Instantaneous spanwise vorticity in the (x, y) plane.

However, the picture changes significantly at the onset of transition. At a certain stage the free shear layer formed in the bubble becomes inviscidly unstable owing to small disturbances imposed in the early stages of the simulation, breaking the strong vortical structures that formed toward the end of the bubble into smaller vortical structures as the first sign of two-dimensional instability and vortex shedding. The shear layer becomes more unstable and the newly formed structures break up again, with coherent 3D structures appearing. A general view of the instantaneous flow field of the transition bubble at time step 93 000 is shown in Figures 7(c), and (d).

After the flow reaches a statistically stationary state, the transition process is clearly visible (Figure 8) which shows the instantaneous spanwise vorticity at various times (1000 time steps interval) in the (x, y) plane at $z/h = 2$ (centre of the computational domain). The vorticity at different z-planes looks very similar. In the beginning of the bubble a free shear layer develops and 2D spanwise vortices form; these are inviscidly unstable *via* the Kelvin–Helmholtz (K–H) mechanism and any small disturbances present grow downstream with an amplification rate larger than that in the case of viscous instabilities. Further downstream, the initial spanwise

DOI: 10.1002/fld

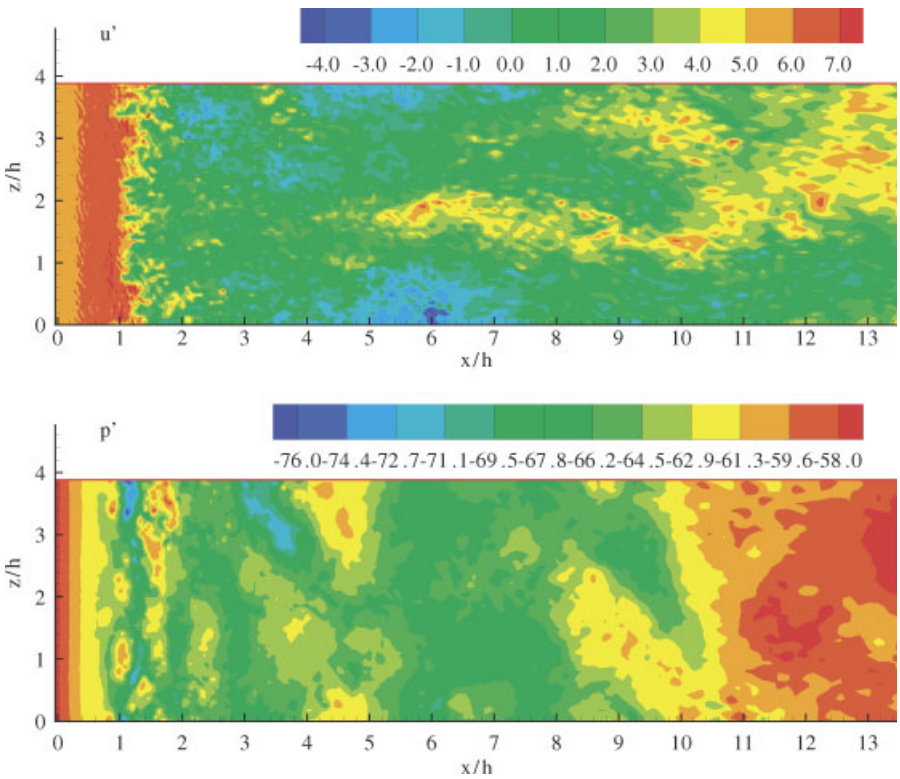

Figure 9. Contours of axial velocity and pressure fluctuations at plan views immediately above the obstacle (at $y/h = 1.04$).

vortices are distorted severely and roll up, leading to streamwise vorticity formation associated with significant 3D motions, eventually breaking down into relatively smaller turbulent structures before the reattachment point and rapidly developing into a turbulent boundary layer subsequently. It is noticeable that the region $0 \leqslant x/h \leqslant 6$, $-1 \leqslant y/h \leqslant 0$ is almost free from any traces of the spanwise vorticity; an indication that either a 'dead region' exists (characterized by very low velocity variations) or the entrainment (mixing rate) is very low and hence almost a laminar region. Looking back at the instantaneous velocity vectors shown in Figure 7(c), it is clear that the region between $0 \leqslant x/h \leqslant 2.5$ is occupied primarily by a counter-rotating vortex (clearly identified from the mean vectors shown in Figure 2(c)) followed by a strong back flow between $2.5 \leqslant x/h \leqslant 6$. Flow visualization (discussed in Section 4) has shown that the flow is dominated by 2D K–H rolls which will only come into contact with the lower surface between $6 \leqslant x/h \leqslant 8$ leaving the region immediately downstream of the obstacle and up to $x/h = 8$ with very little mixing.

The 2D nature of the flow at the separation edge and for a short distance downstream can also be clearly observed from the plan views for both the axial velocity and pressure fluctuations contours immediately above the obstacle height (Figures 9(a) and (b), respectively).

DOI: 10.1002/fld

4. TURBULENCE SPECTRA

4.1. Spectra points selection

To investigate the shedding phenomena for the obstacle case carefully, extensive data of velocity and pressure fields were calculated at 31 points covering the whole computational domain (Figure 10). The distribution of the points are either *clos*e to the surface, at the *edge* or at the *center* of the shear layer. In the present study, the centre of the shear layer is defined as the y-location where the *rms* value of the streamwise velocity (u_{rms}) attains a maximum value, consistent with the definition of Kiya and Sasaki [11]. The edge of the shear layer is defined as the locus of points where u_{rms}/U_0 has a value of 2.5%. This definition is consistent with the experimental studies of Dijalali and Gartshore [35] and Cherry *et al.* [36]. In the current case, few samples are collected to approximate the position of the edge and the centre of the shear layer prior to sample collection for the spectra analysis.

Kiya and Sasaki [11] believe that the low-frequency motion is noticeable close to the separation point rather than downstream locations because the cross-sectional dimensions of the rolled-up vortices are much larger than the spatial extent of the flapping of the shear layer further downstream of the separation line. For this reason 3 points are located immediately upstream of the separation line (1, 2, 3 in Figure 10 and Table I). The spanwise location of these points is at the centre of the computational domain ($z/h = 2.0$).

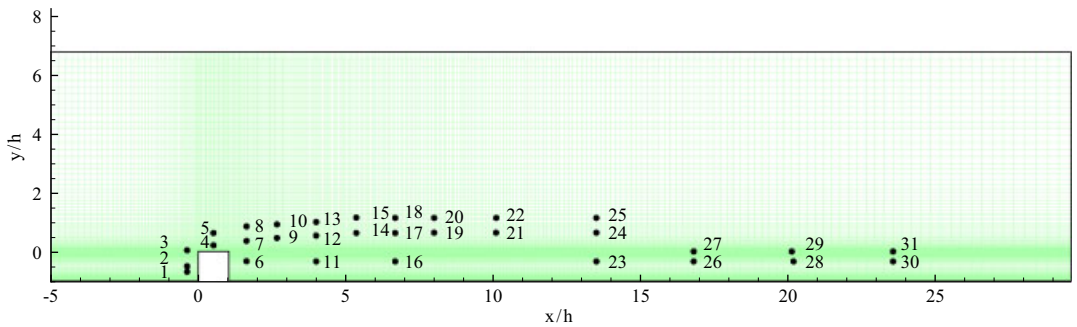

Figure 10. Locations of points for spectral analysis.

Table I. Spectra points coordinates.

Point	1	2	3	4	5	6	7	8	9	10	11
x/h	−0.375	−0.375	−0.375	0.5	0.5	1.65	1.65	1.65	2.7	2.7	4
y/h	−0.7	−0.5	0.04	0.2	0.65	−0.33	0.4	0.85	0.46	0.92	−0.335
Point	12	13	14	15	16	17	18	19	20	21	
x/h	4	4	5.36	5.36	6.7	6.7	6.7	8	8	10	
y/h	0.54	1.0	0.63	1.15	−0.335	0.63	1.14	0.64	1.14	0.64	
Point	22	23	24	25	26	27	28	29	30	31	
x/h	10	13.5	13.5	13.5	16.8	16.8	20.2	20.2	23.6	23.6	
y/h	1.14	−0.335	0.64	1.14	−0.335	0.0	−0.335	0.0	−0.335	0.0	

DOI: 10.1002/fld

A total of 24 990 samples at each point taken every 10 time-steps with time step $= 4.75 \times 10^{-6}$ s (sampling frequency 21.053 kHz) were collected. This corresponds to a total period of 1.187025 s. Both the traditional Fourier transform and the evolving wavelet transform methods were used to process the time series signals of the velocity and pressure fields. At this point it is worth highlighting the advantages and disadvantages of these two methods.

4.2. Windowed Fourier transform (WFT) and wavelet transform

It is common practice to extract the local-frequency information from a signal using the Fourier transform. The Fourier transform is performed on a segment of length T from a time series of time step δt and a total length $N\delta t$, thus returning the frequencies from T^{-1} to $(2\delta t)^{-1}$. The segment can be windowed with an arbitrary function or a Gaussian window (Kaiser [37]). Kaiser [37] argued that the windowed Fourier transform (WFT) represents an inaccurate and inefficient method of time-frequency localization, as it imposes a scale or 'response interval' T into the analysis. The inaccuracy arises from the aliasing of high- and low-frequency components that do not fall within the frequency range of the window. The inefficiency comes from the $T/2\delta t$ frequencies, which must be analysed at each time step, regardless of the window size or the dominant frequencies present. In addition, several window lengths must usually be analysed to determine the most appropriate choice.

The spectra of transitional/turbulent flow usually contain a range of frequencies. In applications where vortex shedding or pairing is involved there might be more than one dominant frequency. For analysis where a predetermined scaling may not be appropriate because of a wide range of dominant frequencies (such as signals resulting from a transitional/turbulent flows), a method of time-frequency localization that is scale dependent, such as *wavelet analysis*, might be more successful and has been considered in this study.

The *wavelet transform* can be used to analyse time series that contain non-stationary powers at many different frequencies (Daubechies [38]). For a time series, x_n, with equal time spacing δt *and* $n = 0, \ldots, N-1$, consider a wavelet function, $\Psi_0(\eta)$ that depends on a non-dimensional 'time' parameter η. To be *admissible* as a wavelet, this function must have zero mean and be localized in both time and frequency space (Farge [39]). An example is the Morlet wavelet, consisting of a plane wave modulated by a Gaussian

$$\Psi_0(\eta) = \pi^{-1/4}\, \mathrm{e}^{\mathrm{i}\omega_0\eta}\, \mathrm{e}^{-\eta^2/2} \tag{19}$$

where ω_0 is the non-dimensional frequency, taken to be 6 to satisfy the admissibility condition (Farge [39]).

'Wavelet function' usually refers to either *orthogonal* or *non-orthogonal* wavelets. The use of an orthogonal basis implies the use of the *discrete wavelet transform*, while a non-orthogonal wavelet function can be used with either the discrete or the *continuous wavelet transform* (Farge [39]). The method used in the current analysis (based on the code developed by Torrence and Compo [40]), employs the continuous transform, although all of the results for significance testing, smoothing in time and scale, and cross-wavelets are applicable to the discrete wavelet transform.

The continuous wavelet transform of a discrete sequence x_n is defined as the convolution of x_n with a scaled and translated version of $\Psi_0(\eta)$

$$W_n(s) = \sum_{n'=0}^{N-1} x_{n'} \Psi^* \left[\frac{(n'-n)\delta t}{s} \right] \tag{20}$$

DOI: 10.1002/fld

where the (*) indicates the complex conjugate. This indicates that the transform is divided into real and imaginary parts or the 'amplitude' and 'phase'. The amplitude is taken as $|W_n(s)|$ and the *wavelet power spectrum* is defined as the absolute value squared of the wavelet transform ($|W_n(s)|^2$) and gives a measure of the time series variance at each scale (period) and at each time. Thus, by varying the *wavelet scale s* and translating along the localized time index *n*, one can construct a picture showing both the amplitude of any features *versus* the scale (period) and how this amplitude varies with time.

Both of the methodologies mentioned above were used here to elucidate the frequency contents of the extensive time series for the velocity and pressure fields. A well tested code utilizing the WFT methods for auto-correlation is used to process the data. The Hanning window (famous for its smallest aliasing error) is used in the WFT code. The code divides the data into segments each of magnitude 2^n. The power factor n should be selected dependent on the number of samples collected (usually 13) which will automatically define the resolution frequency as $1/(2^n \times \delta t)$. However, if the number of samples is small, then n might take a smaller value. In the current case, $n = 13$ resulting in 3 blocks and a frequency resolution of the data is 2.57 Hz. The maximum frequency that can be resolved is 10.526 kHz.

For the wavelet transform, the Morlet wavelet is used, and the transform is performed in Fourier space using the method described in Torrence and Compo [40]. Other wavelet bases, such as the Paul and Mexican hat, were tested and gave the same qualitative results. The wavelet scale s is almost identical to the corresponding Fourier period of the complex exponential, and the terms '*scale*' and '*period*' will be used synonymously. A code developed by Torrence and Compo [40] was modified to perform the analysis for the time series signals shown in this section.

Another important parameter in wavelet analysis of any time series is the choice of scales. Once a wavelet function is chosen, it is necessary to choose a set of scales s to use in the wavelet transform described by relation (20). The scales are usually written as fractional powers of 2 as

$$S_j = S_0 2^{j\delta j}, \quad j = 0, 1, \ldots, J \tag{21}$$

$$J = \delta j^{-1} \log_2(N \delta t / S_0) \tag{22}$$

where S_0 is the smallest resolvable scale, which should be chosen so that the equivalent Fourier period is approximately $2\delta t$ and J determines the largest scale. The choice of a sufficiently small δj depends on the width in spectral-space of the wavelet function. For Morlet wavelet, a δj of about 0.5 is the largest value that still gives adequate sampling in scale [40]. A smaller value of δj gives finer resolution, and in the current analysis $\delta j = 0.25$. The largest scale, J, is taken as 48, giving a total of 49 scales ranging from approximately zero to 0.327 s. Note that relation (22) estimates J as 52, however, this value does not add any significant contents in the wavelet power spectra. Finally, in applying the wavelet analysis for any time signals, it is recommended by Torrence and Compo [40] that the Fourier transform should be performed first and used as a guidance to explain the wavelet power spectra. It is worth pointing out that when applying wavelet analysis for time signals from a turbulence field, then objectivity and care should be considered to avoid misleading results. The selection of the variables mentioned above appeared to provide a smooth picture of the wavelet power spectrum and efficiently delineate the content of the signal processed.

4.3. Discussion

Figures 11(a) and (b) show the time signals recorded for the streamwise velocity u and the wall-normal component v for point 3 immediately upstream of the separation point (Figure 10). The

DOI: 10.1002/fld

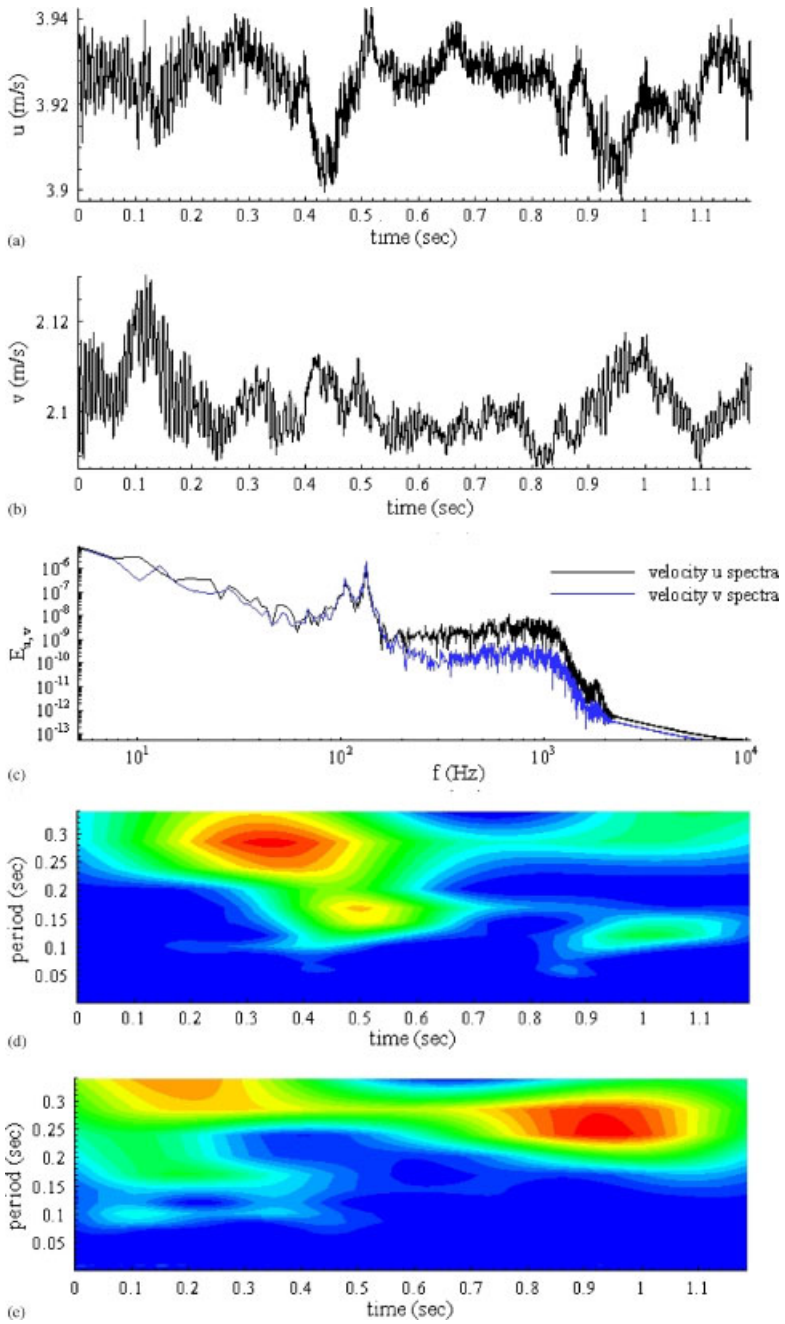

Figure 11. The time series, frequency spectra and wavelet spectra for the velocity components u and v: (a) time signal for u; (b) time signal for v; (c) frequency spectra using WFT; (d) wavelet transform for u; and (e) wavelet transform for v.

DOI: 10.1002/fld

WFT for the two velocity components is shown in Figure 11(c) while the wavelet transform for u and v appear in Figures 11(d) and (e), respectively. In Figures 11(d) and (e), the vertical axis is the period which is equivalent to the scales and represents an approximate measure to the Fourier period of the signal. The spectra of points 1 and 2 do not show any frequency content and are not presented here. However, the spectra obtained from the WFT for the velocity u and v of point 3 (Figures 11(c)) clearly show a *sharp* frequency peak (band) centred at approximately 105 Hz for both velocity components. This is equivalent to (a normalized value of) $5.425(U_0/x_R)$.

The wavelet power spectrum for the velocity component u (Figure 11(d)) shows a clear concentration that most likely corresponds to the frequency peak displayed in Figure 11(c) with additional details. The wavelet power spectra contours give two important pieces of information. The wavelet power contours show that most of the power is concentrated within a band of 0.2–0.33 s ($0.2 \leqslant \text{period} \leqslant 0.33$), although there is a small power concentration at shorter periods ($0.1 \leqslant \text{period} \leqslant 0.2$) which seems to be associated with the first band. The wavelet power spectrum also shows the variation of the frequency of occurrence and amplitude of the signal processed. In this regard, Figure 11(d) clearly shows that the high power concentration occurred in the time between $0.175 \leqslant t \leqslant 0.5$ (centred at $t = 0.35$) and the other event associated with the first band having lower amplitude and occurs in a shorter period $0.45 \leqslant t \leqslant 0.55$. The figure also show there is another power content within the time span of the signal but with lower amplitude and narrower and lower bands. It also indicates that within the time span of the time signal, the event (with higher power content) is not repeated, though towards the end of the time there is evidence that it might repeat itself (i.e. the cycle behaviour of the mechanism responsible for the event). If the samples have been collected over a sufficient long time period, there is a high possibility that the contours might show the possible re-occurrence of the high power concentration event as Figure 11(d) indicates. In fact, the wavelet power spectrum is an exact interpretation to the time signals. Compared to the time signal (Figure 11(a)), it is clear that whenever there is a peak in the velocity magnitude shown by the time signals, it is captured in the wavelet power spectrum at the same time, with the representative amplitude of the signal.

The WFT spectra for the normal velocity v are similar to that of the streamwise velocity component u (Figure 11(c)). The peak of the frequency is at the same value for u. However, the wavelet spectra shown in Figure 11(e) display a slightly different picture. The wavelet spectra show that the power is concentrated at two overlapping bands; the first is $0.275 \leqslant \text{period} \leqslant 0.33$ and the other at a lower band, specifically $0.2 \leqslant \text{period} \leqslant 0.3$. The first power concentration took place between $0.025 \leqslant t \leqslant 0.3$ and the other power concentration occurred later during the time-span of the signal, at $0.7 \leqslant t \leqslant 1.1$. Comparing the power contents in the wavelet spectra to the time series (v signal Figure 11(b)), it is clear that the wavelet spectra have interpreted the time signal correctly. There are two clear peaks in the time signal for the normal velocity v, the first is centred at $t = 0.1$ s and the other is centered at $t = 0.98\,s$ and they are clear in the power spectra in Figure 11(e). The WFT does not show two amplified frequencies but only one. Because the wavelet analysis method used here is strongly connected to WFT methods, the only way to interpret the two power concentration shown in Figure 11(d) is that they correspond to the same event (frequency peak) displayed by the WFT transform. The fact that they happened at two distinctively separated times indicates the frequency of occurrence of this event in time. This shows that the total time of the signal in this study is sufficient for the velocity v peaks to reoccur.

From the discussion of these two spectra, it is clear that the wavelet power spectra provide only qualitative results (many criticise the method for this feature). However, it does give a clear picture of the extent of the event (amplitude) and any smaller events associated with it; and above

DOI: 10.1002/fld

all it gives an indication of the point in time at which the event occurs, and the approximate period needed for the event to reoccur. This information could be useful in controlling such events (damping or exciting as required for specific applications).

It is the trend in almost all the work done in separated–reattached flow that frequency peaks in the region close to the separation line are attributed to the flapping of the shear layer. However, the normalized value is much higher than the corresponding value of what is termed low-frequency motion, observed in separated–reattached flow in different geometries (mainly the blunt plate geometry and the backward-facing step) which is in the range of $0.1U_0/x_R \leqslant f \leqslant 0.18U_0/x_R$. The high normalized value in the current case is partly due to the longer mean reattachment length for the transitional flow under study (when compared to those mentioned in the literature and for which this range applies).

Moreover, it was reported by Castro [20] that if the backflow velocity is small compared to the free-stream velocity (typically less than 20%), the low-frequency component is generally absent. With reference to the mean velocity profiles shown at Figure 4, the maximum backflow velocity rarely exceeds 15% of the free-stream velocity. On further investigation to the mean and instantaneous flow fields at other positions within the recirculation flow downstream and upstream the obstacle (at different times), the maximum back flow was not found to exceed the value mentioned above. Hence, the only possible explanation for this amplified frequency is due to the K–H instabilities in the shear layer forming as a result of the small upstream separated region (the standing vortex). The distinction of this flow compared with the rest of the geometries mentioned here (the blunt plate and the backward-facing step) is that none of them is characterized with a recirculation region upstream of the separation line. A closer look at the nature of the standing vortex is revealed by (z–y) slices of the instantaneous vectors shown in Figures 12(a) (at $x/h = -0.75$) and (b) (at $x/h = -0.425$). The instantaneous vectors show systems of small-scale pairs of counter rotating vortices forming systems of the well known λ-shaped vortices dominating the recirculation region upstream of the obstacle (the standing vortex). Close to the upstream side of the obstacle, the height of the vortices can be seen to reach $y/h \approx 0.75$. These vortices start to build from $2.5h$ distance upstream of the obstacle (the length of the recirculation region upstream of the obstacle, Figure 2), and collide with the upstream side of the obstacle.

In the numerical study of the instability mechanism in transitional separating–reattaching flow for a blunt plate geometry, Abdalla and Yang [28] proved that the boundary layer is indeed unstable *via* the K–H instability mechanism and the value of the Strouhal number based on the plate thickness, freestream velocity and the characteristic frequency observed is in the range $0.225 \leqslant St \leqslant 0.275$. In the current study, the Strouhal number based on the obstacle height, the free stream velocity and the observed frequency ($St = fh/U_0$) is equivalent to $St = 0.242$. This is comparable to the value of $0.225 \leqslant St \leqslant 0.275$ reported by Abdalla and Yang [28] which is further evidence that the observed frequency in the current case is due to K–H instability mechanism.

Figures 13(a) and (b) are the WFT spectra and the wavelet spectra, respectively, for the pressure at point 4 (Figure 10). The WFT frequency spectra does show a broad clear peak centred at $f = 500$ Hz (normalized value $f\theta/U_\infty \approx 0.028$, where θ is the momentum thickness at separation). In turn, the corresponding wavelet power spectra display a clear power concentration which indicates that the signal peak took place at $0.5 \leqslant t \leqslant 0.8$ s although its effects (smaller amplitudes surrounding the peak) span almost the whole life span of the signal ($0.15 \leqslant t \leqslant 1.05$). The power concentration is at a band of $0.25 \leqslant \text{period} \leqslant 0.34$ and it is favourable to associate this event with the peak frequency shown by the corresponding WFT spectra. This value of frequency is comparable to that of the most amplified free shear-layer disturbances in the linear instability theory. A comparable

DOI: 10.1002/fld

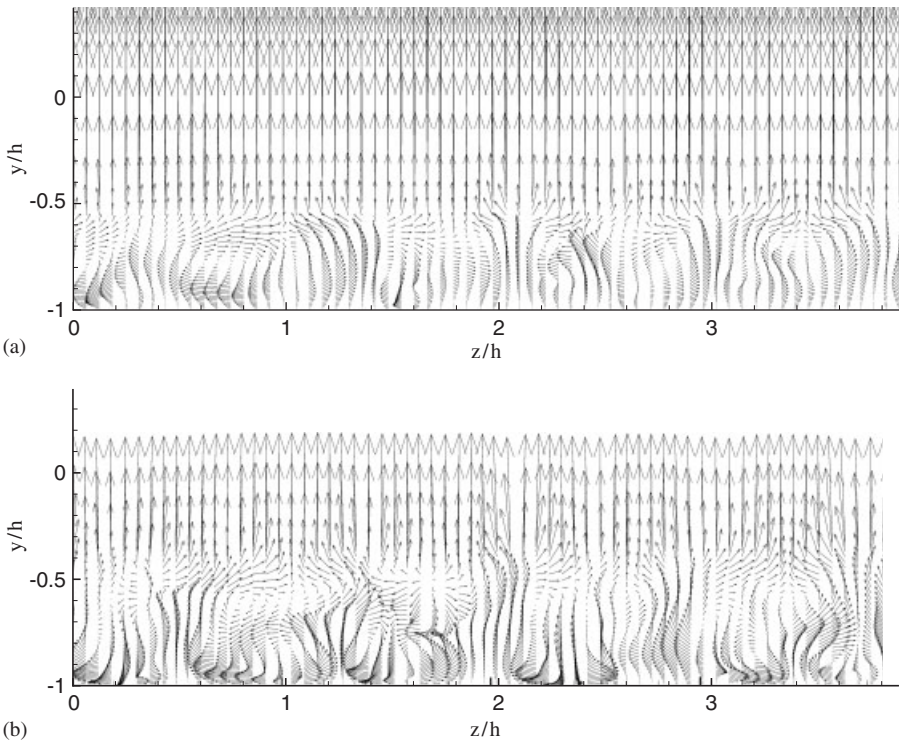

Figure 12. Instantaneous vectors (y–z)-slices at two different locations immediately upstream of the obstacle revealing pairs of counter-rotating vortices: (a) $x/h = -0.75$; and (b) $x/h = -0.425$.

value of $f\theta/U_\infty = 0.016$ was reported by Dovgal [41] for the unexcited laminar separation bubble behind a 2D bump on a flat-plate surface at low Reynolds number ($Re = 2120$). This is likely to be due to the interactions of the shed K–H rolls with the solid surface of the obstacle. In addition to this main power concentration, other events (with less amplitude) can be seen in the wavelet power spectrum mainly at $0.25 \leqslant t \leqslant 0.5$ and at $0.9 \leqslant t \leqslant 1.1$ occurring at a narrower and lower band of order $0.1 \leqslant \text{period} \leqslant 0.175$. Such kind of smaller-scale turbulent events are smoothed out in the WFT, an indication to the superiority of the wavelet power spectra method over WFT.

Figure 13(c) shows the WFT frequency spectra for the velocity field (u, v and w) superimposed for point 5. The frequency spectra for the velocity field show a broad band at higher frequency ($f \approx 1000$) which is associated with the power concentration appearing in the wavelet power spectra for the velocity u shown in Figure 13(d). The wavelet indicates that the signal peak started with a lower band ($0.2 \leqslant \text{period} \leqslant 0.25$) between $0.25 \leqslant t \leqslant 0.65$ and gradually spread to a higher band ($0.25 \leqslant \text{period} \leqslant 0.34$) between $0.7 \leqslant t \leqslant 1.1$. Once again such detailed information offered by the wavelet analysis could be quite helpful in understanding the transient evolution of these signals and the dynamics of the coherent structures responsible for their occurrence. Both the WFT and the wavelet power spectra indicate that the amplitude of these events are weak.

Figure 14(a) is an example of the WFT spectra for the velocity field (u, v and w) at point 9 (Figure 10) at the *centre* of the shear layer. The WFT spectra for the rest of the points at the centre

DOI: 10.1002/fld

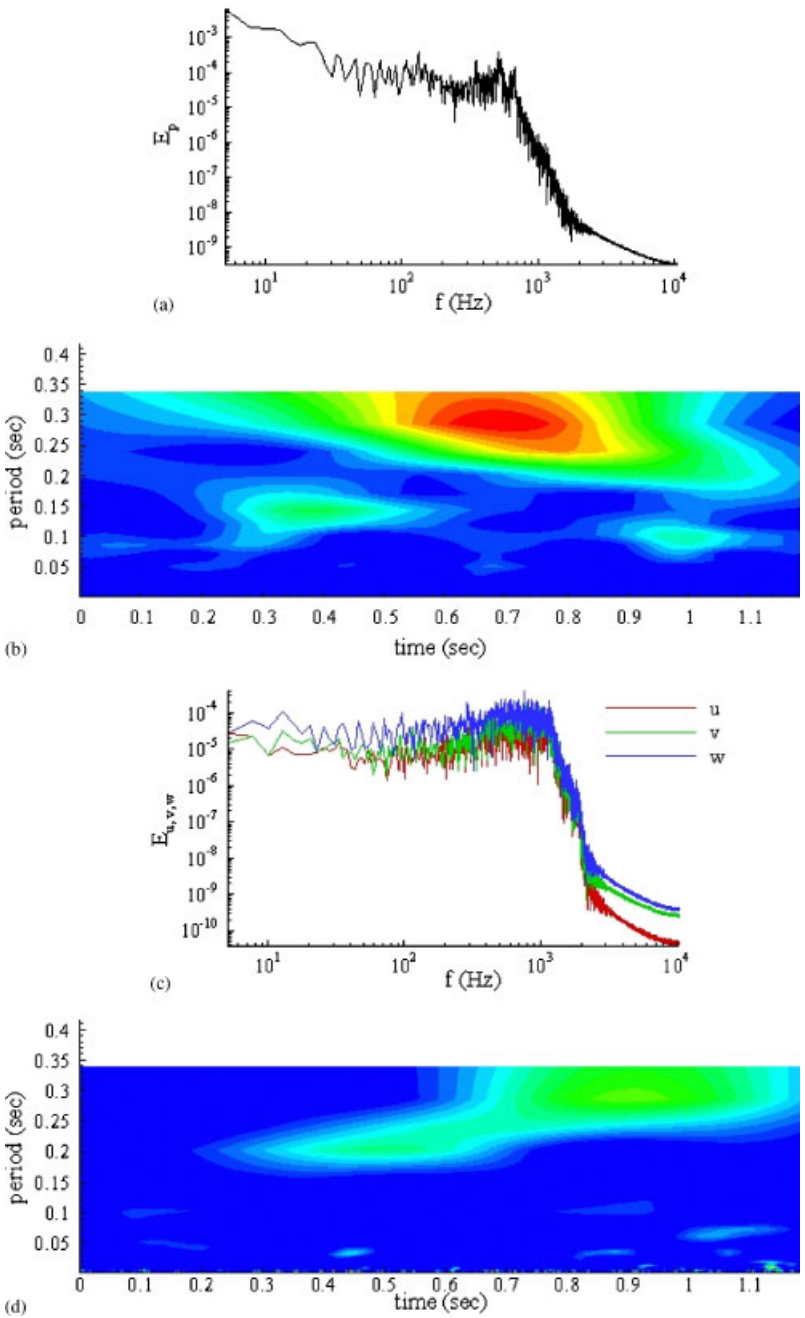

Figure 13. Spectra for points 4 and 5: (a) Fourier transform for the pressure field for point 4; (b) wavelet transform for the pressure field for point 4; (c) Fourier transform for the velocities u, v, and w for point 5; and (d) wavelet transform for the velocities u for point 5.

DOI: 10.1002/fld

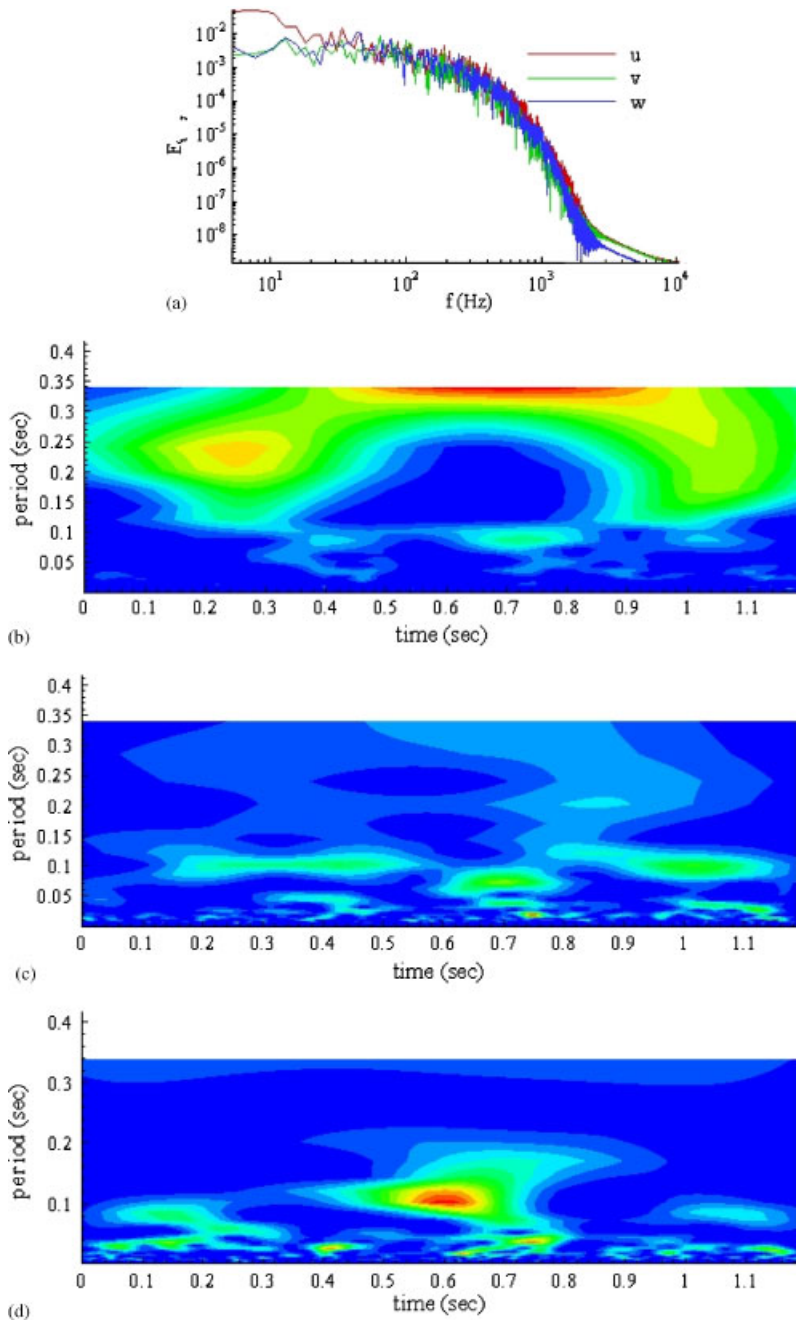

Figure 14. Spectra for the velocity field for point 12: (a) Fourier transform for the velocity u, v, and w; (b) wavelet transform for velocity u; (c) wavelet transform for velocity v; and (d) wavelet transform for velocity w.

DOI: 10.1002/fld

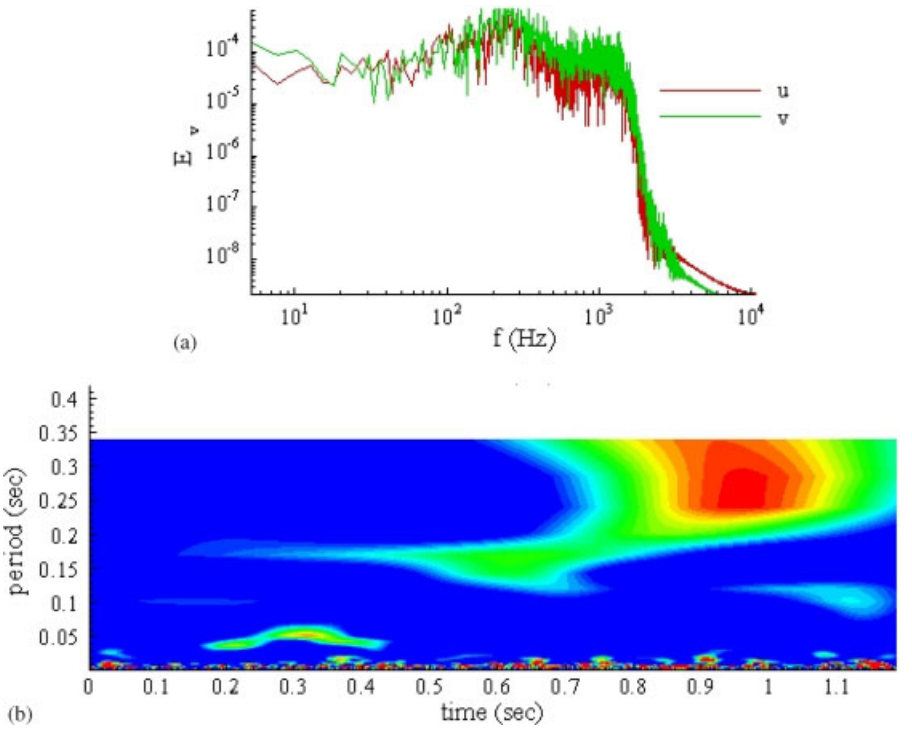

Figure 15. Spectra for velocities u and v at point 8 (edge of the shear layer): (a) Fourier transform for the velocity u, v; and (b) wavelet transform for velocity u.

of the shear layer (points 7, 12, 14, 17, 19, 21 and 24) show similar behaviour. The WFT spectra is quiet and show no details of any peak frequencies and resembles that of a fully developed turbulent boundary layer. Taking into consideration that these points are within a recirculation region, it is expected to contain some amplified frequencies. The wavelet spectra for the velocity u are shown in Figure 14(b). The wavelet power spectra does show two regions of power concentration, both of them at a band $0.125 \leqslant \text{period} \leqslant 0.33$ occurring at times $0.1 \leqslant t \leqslant 35$ and $0.1 \leqslant t \leqslant 35$, respectively. However, the spectra does indicate that the two regions are a continuation of one another (only that the band becomes narrower at $0.5 \leqslant t \leqslant 0.8$), an indication of the uniform distribution of the power throughout the life span of the signal. This is probably the main reason why the WFT does not show any amplified frequencies for the velocity u. However, the wavelet power spectra still provided more detailed information of the signal than the WFT.

The power spectra for the wall-normal velocity component v shown in Figure 14(c) does not show significant contents (only low amplitude power concentration at quite narrow and low bands) and it is not surprising that the WFT counterpart is quiet. The wavelet power spectrum contours of the spanwise velocity w shown in Figure 14(d) indicates that there is a peak at lower bands which occurred in a very short period ($0.45 \leqslant t \leqslant 0.75$) which cannot be distinguished in the WFT. This is a clear indication of the shortcomings of the WFT method in extracting the smaller details and contents of a signal.

Figures 15(a) and (b) show the WFT frequency spectra and the wavelet spectra for the streamwise and wall-normal velocity components u and v for point 8 at the *edge* of the shear layer.

DOI: 10.1002/fld

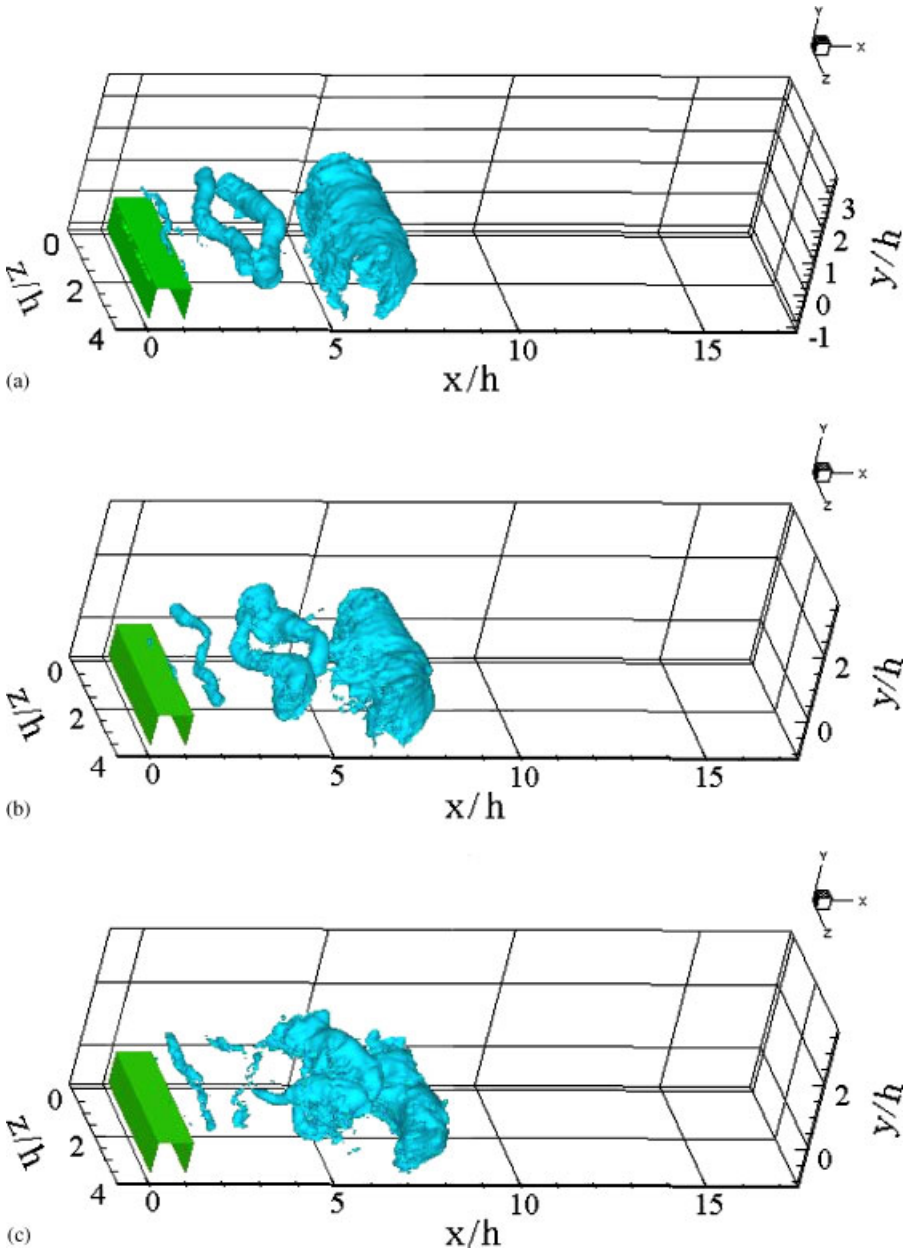

Figure 16. Low-pressure isosurfaces showing Kelvin–Helmholtz rolls undergoing pairing in helical mode at varying times: (a) $t = 0.1615$ s; (b) $t = 0.16625$ s; and (c) $t = 0.171$ s.

The WFT spectra show amplified frequency band centred at $f = 200$ Hz ($St = 0.46$), connected to a broad band at approximately $f = 1000$ Hz. The wavelet spectra shown in Figure 15(b) display power concentration at lower band ($0.15 \leqslant \text{period} \leqslant 0.2$) between $0.45 \leqslant t \leqslant 0.7$ which smoothly

DOI: 10.1002/fld

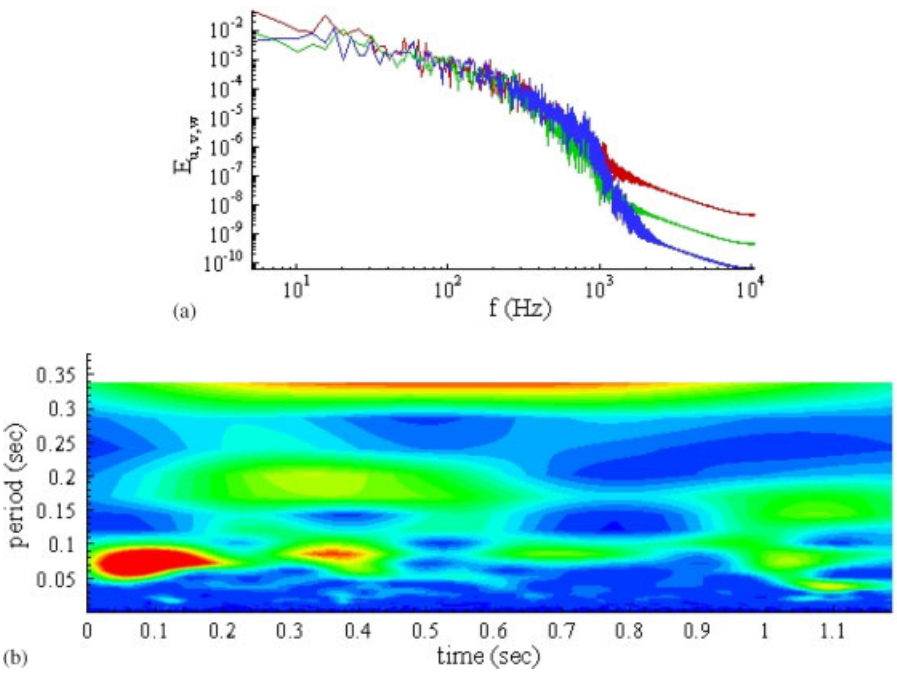

Figure 17. Frequency spectra for the velocity u, v, and w at point 16 close to the lower solid boundary within the recirculation region: (a) WFT frequency for u, v, and w superimposed; and (b) wavelet spectra for u.

spread to a higher band of order $0.25 \leqslant \text{period} \leqslant 0.33$ that took place at $0.75 \leqslant t \leqslant 1.05$ (similar to Figures 13(c) and (d)). It is most likely that the power concentration at the two bands are associated with the peak values noticed in the WFT spectra. This amplified frequency was also barely apparent at points 10 and 13 both at the edge of the shear layer downstream of the separation point. However, it gradually disappears for points 15, 18, 20, 22 and 25 at the edge of the shear layer. The lower frequency ($f = 200\,\text{Hz}$) corresponds to the vortex shedding which originates, in the present case, from the pairing of vortices rolling-up at the fundamental instability frequency of the separating shear layer. This is clearly shown in Figures 16(a)–(c) which visualize the coherent structures in the flow using the low-pressure isosurfaces methodology. The snap shots are taken at three consecutive 1000 time step intervals. The figures show that 2D K–H rolls are shed from the separation line coagulate while convecting downstream. Eventually, such structures collide with the previously shed structure and pair (merge) to form a larger counter part (Figures 16(a) and (b)). The region between the separation line and $8h$ downstream of the separation line is a region where K–H rolls pair and merge to form larger counterparts. They come in contact with the lower solid boundary $8h$ downstream of the separation line (Figures 16(b) and (c)), after which they begin to break down into smaller 3D structures. This could explain why the frequency peak fades for the points while moving downstream of the separation line and especially after $8h$ downstream of the separation line and strengthens the fact that pairing of K–H rolls could be responsible for this frequency peak. It is noticeable that this

DOI: 10.1002/fld

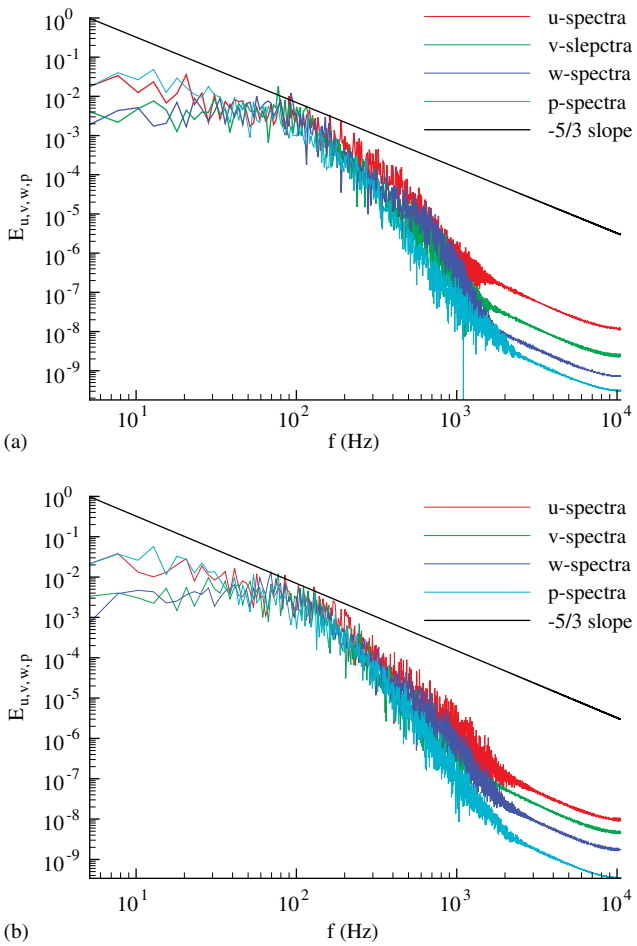

Figure 18. Frequency spectra for the velocity and pressure fields: (a) for point 30; and (b) for point 31. There are compared with the $-\frac{5}{3}$ slope line.

value is almost twice the value reported upstream of the separation and slightly higher than the value of $0.225 \leqslant St \leqslant 0.275$ reported by Abdalla and Yang [14], Kiya and Sasaki [11] and Cherry *et al.* [12] for the separated shear layer behind a blunt plate. Again, the wavelet power spectrum (Figure 15(b)) shows more details than the WFT counterpart. A quite narrow and low banded but clear power concentration appear to have taken place between $0.2 \leqslant t \leqslant 0.4$ which cannot be traced in the WFT spectra. However, overall the flow does not seem to be characterized by a strong shedding phenomena which indicates the quick transition to turbulence in this type of separated–reattached flow.

Figure 17(a) is a sample for the WFT spectra for points within the recirculation region and close to the lower solid boundary (points 6, 11, 16 and 23 in Figure 10). The WFT frequency spectra

DOI: 10.1002/fld

for all these points show a similar trend to the one in Figure 17(a) which is quiet and contains no apparent power concentration. The wavelet power (Figures 17(b)) does not show any distinct features and the power seems uniformly distributed both at low and high bands and throughout the time span of the signal.

Figures 18(a) and (b) are the WFT spectra for the velocity and pressure fields at point 30 and 31 in the developing turbulent boundary layer after the mean reattachment region. The spectra for the rest of the points after the mean reattachment region (points 26, 27, 28, 29) show a similar behaviour. The frequency spectra for both the velocity and pressure field are quiet. It is expected that at this region the boundary layer starts to recover to its canonical form. However, the reason that the spectra do not show a $-\frac{5}{3}$ slope is due to the low turbulence Reynolds number of the flow.

5. CONCLUSIONS

Transitional flow over a surface-mounted obstacle at low Reynolds number was simulated using the LES methodology with a dynamic-subgrid scale model. The mean field including the mean reattachment length and the mean and rms values of the velocity field are in good agreement with the available experimental and DNS data. The discrepancies in the results are attributed to basic differences in the blockage ratio and the transitional nature of the flow.

Extensive studies of the spectra using both the WFT and wavelet power spectrum revealed 3 modes of excited frequencies. The first is of order 105 Hz (corresponding to a Strouhal number $St \approx 0.242$) and detected at points close to the separation line immediately upstream of the obstacle. This value is in agreement with those reported for K–H instability in separated–reattached flow. Due to the low value of the backflow velocity relative to the freestream velocity in the current study, it is concluded that this frequency is due to the K–H instabilities in the shear layer forming in the boundary of the small upstream separated region. The second peak is of order 500 Hz ($f\theta/U_\infty \approx 0.028$) and captured by the pressure field close to the surface of the obstacle. The value is comparable to the most amplified mode of free shear-layer disturbances in the linear instability theory (reported by Dovgal [41] as $f\theta/U_\infty = 0.016$) and attributed in the current case to the interaction of the shed 2D K–H vortices with the solid surface. The third frequency content of the spectra is of order 200 Hz ($St \approx 0.46$), mostly associated with locations at the edge of the shear layer and corresponds to the vortex shedding originating from the pairing of vortices rolling-up at the fundamental instability frequency of the separating shear layer.

The wavelet power spectra have shown compatible results with the WFT but capture more smaller details of the signal than the WFT method. The results indicate that the WFT does not capture the events that take place at narrow bands and those which occur over a short period of time. In contrast, the wavelet spectra reveal the content of the signal regardless of how much narrower the band is or how short the time is over which the event takes place. They also give a qualitative indication of the amplitude of the signal with respect to the dominant noise in the signal. Such detailed knowledge of the contents of a velocity or a pressure field signal in separated–reattached flows is important as it facilitates understanding of the mechanisms behind their existence, the frequency of their occurrence during the signal life-span, their amplitude (strength) and their interaction and development in time. This could be very helpful in

DOI: 10.1002/fld

designing methodologies to control such mechanisms (damping or exciting as required) to satisfy the application purpose.

ACKNOWLEDGEMENTS

The computations were carried out on a LINUX cluster in the Department of Computing Sciences and Engineering at De Montfort University. The authors are grateful to Drs Antonio Cau and Paul Cropper for their assistance and support in using this facility.

NOMENCLATURE

C	Smagorinsky model constant
E_p	pressure spectra
E_{U}	streamwise velocity spectra
E_{V}	wall-normal velocity spectra
E_{W}	spanwise velocity spectra
h	obstacle height
H	channel height
i	streamwise axis index
J	largest resolvable scale (wavelet)
j	wall-normal axis index
k	spanwise axis index
l	obstacle width
N	total number of samples
p'	pressure fluctuation
S_0	smallest resolvable scale (wavelet)
St	Strouhal number
s	wavelet scale
$\bar{U}$	mean streamwise velocity
U_0	freestream velocity
u'	axial velocity fluctuation
u_{rms}	rms value of the streamwise velocity
v_{rms}	rms value of the wall-normal velocity
x	streamwise axis
x_{R}	mean reattachment length
y	wall-normal axis
z	spanwise axis
Δx^+	wall-normal mesh size in wall units
Δy^+	streamwise mesh size in wall units
Δz^+	spanwise mesh size in wall units
δ	boundary layer thickness
v	total viscosity
θ	momentum thickness
λ	time parameter for wavelet function
Ψ_0	Morlet wavelet

DOI: 10.1002/fld

REFERENCES

1. Bergeles G, Athanassiadis N. The flow pass a surface mounted obstacle. *Journal of Fluid Engineering* (ASME) 1983; **105**:461–463.
2. Castro IP. Relaxing wakes behind surface-mounted obstacles in rough wall boundary layers. *Journal of Fluid Mechanics* 1979; **93**:631–659.
3. Durst F, Rastogi AK. Turbulent flow over two-dimensional fences. In *Turbulence Shear Flows*, vol. 2. Springer: Berlin, 1980; 218–231.
4. Dimaczek G, Kessler R, Martinuzzi R, Tropea C. The flow over two-dimensional surface-mounted obstacles at high Reynolds numbers. *Turbulence Shear Flow VII*. 1989; **1**(A90-35176 15-34):10.1.1–10.1.6.
5. Tropea CD, Gackstatter R. The flow over two-dimensional surface-mounted obstacles at low Reynolds number. *Journal of Fluids Engineering* 1984; **107**:489–494.
6. Yang KS, Ferziger JH. Large eddy simulation of turbulent obstacle flow. Using a dynamic subgrid-scale model. *AIAA Journal* 1993; **31**:1406–1413.
7. Orellano A, Wengle H. Numerical simulation (DNS and LES) of manipulated turbulent boundary layer flow over a surface-mounted fence. *European Journal of Mechanics B-Fluids* 2000; **19**:765–788.
8. Larsen PS. Database on tc-2C and tc-2D fence-on-wall and obstacle-on-wall test case. *Report AFM-ETMA 95-01*, Denmark, TU, 1995. (ISSN 0590-8809).
9. Lee S, Bienkiewicz B. Large-eddy simulation of wind effects on bluff bodies using the finite element method. *Journal of Wind Engineering and Industrial Aerodynamics* 1997; **67–68**:601–609.
10. Werner H, Wengle H. Large-eddy simulation of the flow over a square rib in a channel. *Proceedings of Seventh Symposium on Turbulent Shear Flows*, Stanford University, 1989; 10.2.1–6.
11. Kiya M, Sasaki K. Structure of a turbulent separation bubble. *Journal of Fluid Mechanics* 1983; **137**:83–113.
12. Cherry NJ, Hillier R, Latour MEP. The unsteady structure of two-dimensional separated and reattaching flows. *Journal of Wind Engineering and Industrial Aerodynamics* 1983; **11**:95–105.
13. Tafti DK, Vanka SP. Numerical study of flow separation and reattachment on a blunt plate. *Physics of Fluids A* 1991; **3**(12):2887–2909.
14. Abdalla IE, Yang Z. Numerical study of a separated—reattached flow on a blunt plate. *AIAA Journal* 2005; **43**:2465–2474.
15. Castro IP, Haque A. The structure of a turbulent shear layer bounding a separation region. *Journal of Fluid Mechanics* 1987; **179**:439–468.
16. Laura MH, Ahmed MN. Wall-pressure-array measurements beneath a separating/reattaching flow region. *40th Aerospace Sciences Meeting and Exhibit*, Reno, NV, 2002; 14–17.
17. Ruderich R, Fernhholz HH. An experimental investigation of a turbulent shear flow with separation, reverse flow and reattachment. *Journal of Fluid Mechanics* 1986; **163**:283–322.
18. Eaton JK, Johnston JP. Low frequency unsteadiness of a reattaching turbulent shear layer. In *Turbulence Shear Flows*, Bradbury LJS, Durst F, Launder BE, Schmidt FW, Whitelaw JH (eds), vol. 3. Springer: Berlin, 1982; 162–170.
19. Lee I, Sung HJ. Characteristics of wall pressure fluctuations in separated and reattaching flow over a backward-facing step. *Experiments in Fluids*, vol. 30. Springer: Berlin, 2001; 262–272.
20. Castro IP. The stability of laminar symmetric separated wakes. *Journal of Fluid Mechanics* 2005; **532**:389–411.
21. Alam M, Sandham ND. Direct numerical simulation of 'short' laminar separation bubbles with turbulent reattachment. *Journal of Fluid Mechanics* 2000; **410**:1–28.
22. Germano M, Piomelli U, Moin P, Cabot WH. A dynamic sub-grid scale eddy viscosity model. *Physics of Fluids* 1991; **A3**(7):1760–1765.
23. Lilly DK. A proposed modification of the Germano subgrid-scale closure method. American Institute of Physics. *Physics of Fluids A* 1992; **4**:633–635.
24. Smagorinsky J. General circulation experiments with the primitive equations. *Monthly Weather Review* 1963; **91**:99–164.
25. Ferziger J, Peric M. *Computational Methods for Fluid Dynamics* (2nd edn). Springer: Berlin, Heidelberg, 1998.
26. Harlow FH, Welch JE. Numerical calculations of time dependent viscous incompressible flow of fluid with a free surface. *Physics of Fluids* 1965; **8**(12):2182–2189.
27. Abdalla IE. Numerical studies of separated boundary layer transition on a flat plate with a blunt leading edge. *Ph.D. Thesis*, Loughborough University, Loughborough, 2004.
28. Abdalla IE, Yang Z. Numerical study of the instability mechanism in transitional separating-reattaching flow on a blunt plate. *International Journal of Heat and Fluid Flow* 2004; **25**(4):593–605.

DOI: 10.1002/fld

29. Abdalla IE, Yang Z. Computational visualisation of separated-reattached transitional flow on a blunt plate. *Journal of Flow Visualisation and Image Processing* 2004; **11**:1–28.
30. Yang Z, Abdalla IE. Effects of free-stream turbulence on large-scale coherent structures of separated boundary layer transition. *International Journal for Numerical Methods in Fluids* 2005; **49**:331–348.
31. Yang Z, Voke PR. Large-eddy simulation of boundary-layer separation and transition at a change of surface curvature. *Journal of Fluid Mechanics* 2001; **439**:305–333.
32. Hung Le, Parviz M, Kim J. Direct numerical simulation of turbulent flow over a backward-facing step. *Journal of Fluid Mechanics* 1997; **330**:349–374.
33. Tillman W. Investigation of some particulars of turbulent boundary layers on plates. *British Ministry of Aircraft Production* 1945; MAP-VGG-34-45T.
34. Castro IP, Fackrell JE. A note on two-dimensional fence flows with emphasis on the wall constraint. *Journal of Industrial Aerodynamics* 1978; **3**:1–20.
35. Djilali N, Gartshore IS. Turbulent flow around a bluff rectangular plate. Part I: Experimental investigation. *Journal of Fluids Engineering* (ASME) 1991; **113**:51–59.
36. Cherry NJ, Hillier R, Latour MEP. Unsteady measurements in a separated and reattaching flow. *Journal of Fluid Mechanics* 1984; **144**:13–46.
37. Kaiser G. *A Friendly Guide to Wavelets*. Birkhäuser: Cambridge, MA, 1994.
38. Daubechies C. The wavelet transform time-frequency localization and signal analysis. *IEEE Transactions on Information Theory* 1990; **36**(5):961–1005.
39. Farge M. Wavelet transforms and their applications to turbulence. *Annual Review of Fluid Mechanics* 1992; **24**:395–457.
40. Torrence C, Compo GP. A practical guide to wavelet analysis. *Bulletin of the American Meteorological Society* 1998; 61–77.
41. Dovgal AV. Non-stationarity of laminar separation bubble modified by periodic excitation. *Russian Journal of Engineering Thermophysics* 1999; **9**(4):285–296.

DOI: 10.1002/fld